

# Learning Task-Specific Strategies for Accelerated MRI

Zihui Wu<sup>1</sup>, Tianwei Yin<sup>2</sup>, Yu Sun<sup>1</sup>, Robert Frost<sup>3</sup>, Andre van der Kouwe<sup>3</sup>  
Adrian V. Dalca<sup>2,3</sup>, Katherine L. Bouman<sup>1</sup>

**Abstract**—Compressed sensing magnetic resonance imaging (CS-MRI) seeks to recover visual information from subsampled measurements for diagnostic tasks. Traditional CS-MRI methods often separately address measurement subsampling, image reconstruction, and task prediction, resulting in a suboptimal end-to-end performance. In this work, we propose TACKLE as a unified co-design framework for jointly optimizing subsampling, reconstruction, and prediction strategies for the performance on downstream tasks. The naive approach of simply appending a task prediction module and training with a task-specific loss leads to suboptimal downstream performance. Instead, we develop a training procedure where a backbone architecture is first trained for a generic pre-training task (image reconstruction in our case), and then fine-tuned for different downstream tasks with a prediction head. Experimental results on multiple public MRI datasets show that TACKLE achieves an improved performance on various tasks over traditional CS-MRI methods. We also demonstrate that TACKLE is robust to distribution shifts by showing that it generalizes to a new dataset we experimentally collected using different acquisition setups from the training data. Without additional fine-tuning, TACKLE leads to both numerical and visual improvements compared to existing baselines. We have further implemented a learned  $4\times$ -accelerated sequence on a Siemens 3T MRI Skyra scanner. Compared to the fully-sampling scan that takes 335 seconds, our optimized sequence only takes 84 seconds, achieving a four-fold time reduction as desired, while maintaining high performance.

**Index Terms**—Compressed sensing MRI, deep learning, task-specific imaging, end-to-end training.

## I. INTRODUCTION

Compressed sensing magnetic resonance imaging (CS-MRI) is a popular accelerated MRI technology [1]. Commonly, CS-MRI is formulated as an imaging inverse problem where the goal is to recover a high-quality image from its subsampled measurements. Traditional CS-MRI techniques include solving a regularized optimization problem [2]–[5] or training deep learning (DL) models [6]–[8] that recover an image from a pre-determined set of measurements. Recently, a new group of DL-based methods, known as *co-design*, has been proposed to jointly optimize the choice of measurements and a reconstruction module, leading to better reconstruction performance than the traditional CS-MRI methods [9]–[23].

In the existing co-design literature, task prediction is often viewed as a post-processing step decoupled from image reconstruction. All the aforementioned methods focus on image

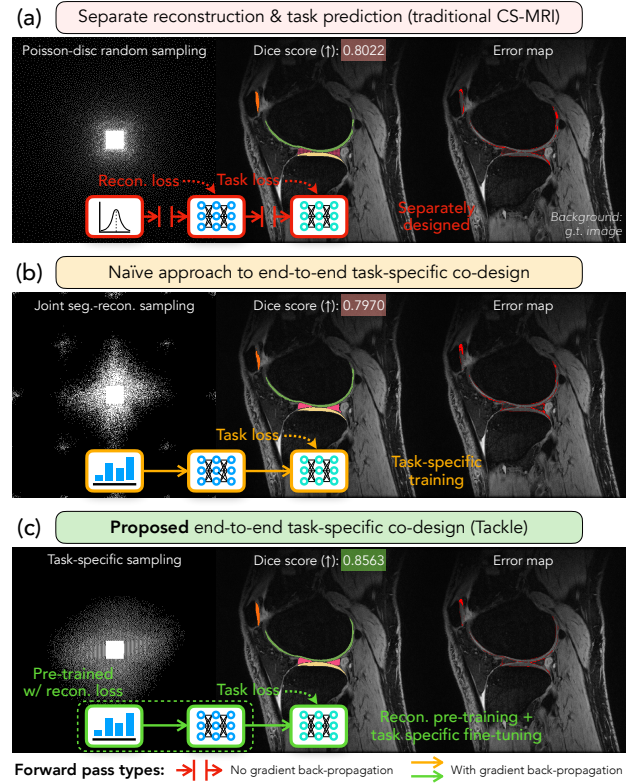


Fig. 1. Comparison between (a) traditional CS-MRI, (b) a naïve approach to task-specific CS-MRI, and (c) the proposed TACKLE framework. Compared with panel (a) that separately deals with reconstruction and task prediction, panel (b) is a simple extension of co-design methods for solving downstream tasks by adding a learnable mapping from measurements to task predictions. However, this naïve approach leads to a suboptimal performance and can even lead to a worse task prediction accuracy, as shown in the example above. On the other hand, we introduce TACKLE for effectively learning task-specific CS-MRI strategies. TACKLE is first pre-trained for generic reconstruction, and then both all three modules are fine-tuned for a more specific downstream task. We find that this training schedule allows TACKLE to robustly learn generalizable task-specific strategies. In the above knee segmentation example, all three approaches are trained with the same architectures for the reconstructor (second module) and predictor (third module). Nevertheless, TACKLE significantly outperforms the two baseline approaches.

reconstruction and rely on standard image similarity metrics such as mean square error (MSE) or peak signal-to-noise ratio (PSNR) as a proxy for performance on a downstream task. Such a reconstruction-oriented formulation lacks a direct connection with the downstream tasks that reflect actual clinical needs [24]. We are thus motivated to ask: *can one improve the accuracy of downstream task prediction by optimizing the entire CS-MRI pipeline in an end-to-end fashion?*

With end-to-end co-design methods, it seems like we are

<sup>1</sup> Department of Computing and Mathematical Sciences, California Institute of Technology, Pasadena, CA 91105, USA.

<sup>2</sup> Computer Science and Artificial Intelligence Lab (CSAIL), Massachusetts Institute of Technology, Cambridge, MA 02139, USA.

<sup>3</sup> Athinoula A. Martinos Center for Biomedical Imaging, Department of Radiology, MGH, Harvard Medical School, Charlestown, MA 02129, USA.

only one step away from incorporating downstream tasks as part of the optimization. Namely, one can simply append a task prediction module and add a task-specific loss. However, as shown in Figure 1 and Table II, this approach leads to a suboptimal performance on the task prediction and is sometimes even worse than the traditional approach of separate reconstruction and task prediction. These results indicate that it remains a challenge on how to robustly learn task-specific strategies for CS-MRI.

In this paper, we address this challenge by proposing a unified framework, *task-specific codesign of k-space subsampling and prediction* (TACKLE), for designing task-specific CS-MRI systems. Different from existing works that focus on specific tasks, TACKLE is a general framework that accommodates different downstream tasks. To do so, we design a two-step training strategy that mimics the training of modern language and vision models. TACKLE is first trained for a generic task of image reconstruction, and then fine-tuned for specific downstream tasks. We find that this approach can effectively learn generalizable task-specific strategies that lead to significant and consistent improvements, with an example shown in Figure 1 (c). Besides the standard task of reconstructing the full FOV (which we call full-FOV reconstruction hereafter), we demonstrate TACKLE on three other tasks covering both pixel-level and image-level imaging problems: region-of-interest (ROI) oriented reconstruction, tissue segmentation, and pathology classification. Our experimental results show that end-to-end optimization for task prediction sometimes circumvents the typical reconstruction in terms of point-wise accuracy, but leads to improved accuracy on the task of interest by effectively extracting key visual information for task prediction.

The main contributions of this work are as follows:

- We provide a general framework (TACKLE) that learns specific strategies for a variety of CS-MRI tasks. TACKLE optimizes the entire CS-MRI pipeline, from measurement acquisition to label prediction, in an end-to-end fashion *directly* for a user-defined task.
- We validate TACKLE on multiple MRI datasets, covering different body parts, scanning sequences, and hardware setups. Experimental results show that TACKLE outperforms the reconstruction-oriented baseline methods on *all* considered settings. We evaluate the proposed end-to-end architecture and training procedure through ablation studies. Our results offer guidance for designing effective task-specific CS-MRI systems in the future.
- We show the generalization of TACKLE to out-of-distribution data by deploying it to a dataset we experimentally acquired using an different acquisition sequence from that of the training data. We further implement a learned 4 $\times$ -accelerated sequence on a Siemens 3T MRI Skyra scanner. The sequence shortens the scan time from 335 seconds to 84 seconds, a four-fold time reduction as desired, while maintaining high performance. These experiments highlight the real-world practicality of our method.

## II. BACKGROUND

### A. Compressed sensing MRI

CS-MRI [1] refers to accelerating MRI via *compressed sensing* (CS) [25], which aims to reconstruct the underlying image from a set of subsampled  $k$ -space measurements.

1) *Basics*: The common setup of CS-MRI involves the reconstruction of an image  $\mathbf{x} \in \mathbb{C}^n$  from its (zero-filled) complex-valued noisy  $k$ -space measurements

$$\mathbf{y} := \mathbf{m} \odot (\mathbf{F}\mathbf{x} + \mathbf{n}) \in \mathbb{C}^n, \quad (1)$$

where  $\mathbf{F}$  is the Fourier transform operator,  $\mathbf{m} \in \{0, 1\}^n$  is the Cartesian subsampling mask,  $\mathbf{n} \in \mathbb{C}^n$  is the complex measurement noise, and  $\odot$  is the element-wise multiplication of two vectors. For parallel imaging MRI, the measurements are collected from multiple coils. For the  $i$ -th coil, the measurements  $\mathbf{y}_i$  can be expressed as

$$\mathbf{y}_i := \mathbf{m} \odot (\mathbf{F}\mathbf{S}_i\mathbf{x} + \mathbf{n}_i) \in \mathbb{C}^n, \quad (2)$$

where  $\mathbf{S}_i$  is the pixel-wise sensitivity map and  $\mathbf{n}_i$  is the measurement noise of the  $i$ -th coil. For both settings, we refer to  $b := \|\mathbf{m}\|_1$  as the sampling budget and  $R := \frac{n}{b}$  as the acceleration ratio of the acquisition. Classical CS-MRI enables sampling below the Nyquist-Shannon rate by solving an optimization problem with a regularizer that leverages the structure of MRI images [2], [26]–[28].

2) *Subsampling patterns*: Subsampling patterns, or masks, in traditional CS-MRI are often generated randomly or hand-crafted to have a point spread function (PSF) with low coherence, which leads to better reconstruction performance according to the CS theory. Popular subsampling patterns include the 2D variable density [1], bidirectional Cartesian [29], Poisson-disc [30], and continuous-trajectory variable density [31], among others [32], [33]. Despite overall effectiveness, these subsampling patterns are designed for generic image reconstruction and not optimized for any specific body part and diagnostic purpose. Therefore, these patterns may lead to suboptimal performance for downstream tasks where specific anatomical or pathological information is relevant.

3) *DL-based reconstruction*: Recently, DL methods have achieved state-of-the-art performance on CS-MRI reconstruction. One line of work combines data-driven priors with model-based iterative reconstruction (MBIR) [3], [4], [34], [35]. Another line of work learns a model-free reconstruction network via end-to-end training [36]–[40]. A third line of work, known as deep unrolling (DU), combines the characteristics of MBIR and end-to-end training [6], [8], [41]–[48]. The idea is to “unroll” an iterative optimization procedure into a cascade of mappings and train these mappings end-to-end so that they can gradually map a low-resolution input image to a high-quality output reconstruction. Inheriting the advantage of both MBIR and end-to-end learning, these methods exhibit state-of-the-art performance on CS-MRI reconstruction. In this paper, we use a specific kind of unrolled network called E2E-VarNet [43] as part of our framework due to its strong performance on the large-scale fastMRI dataset [49].

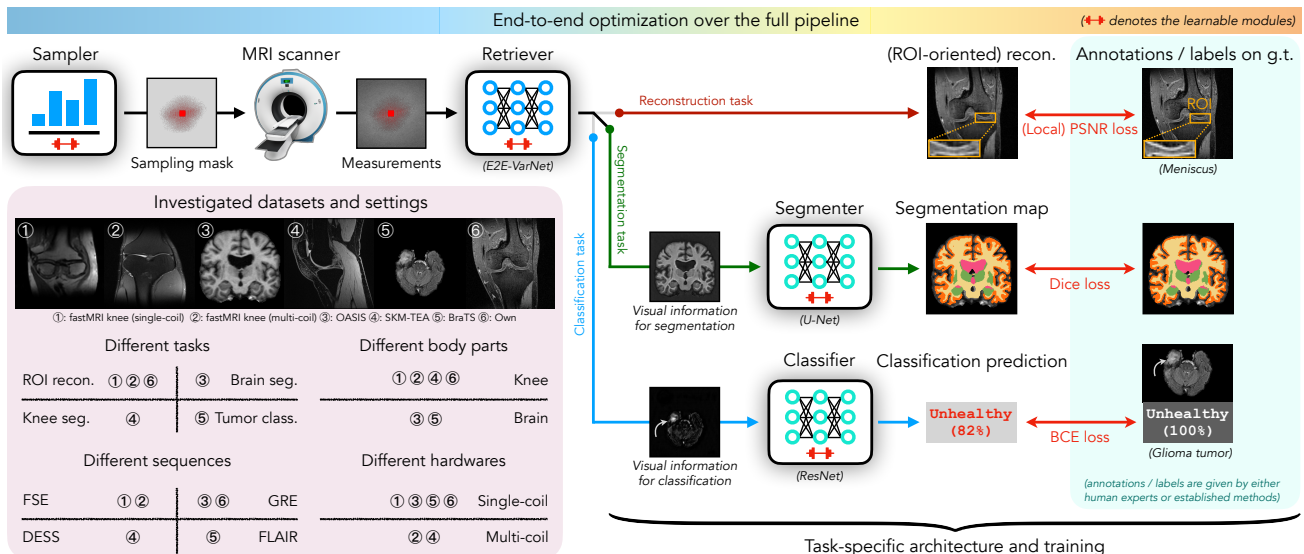
Task-specific co-design of  $k$ -space subsampling and prediction (Tackle)

Fig. 2. Block diagram of the proposed framework TACKLE and a summary of the investigated datasets and settings. TACKLE uses a task-specific loss to jointly optimize a sampler, retriever, and an optional predictor, ranging from scanner-level sampling to human-level diagnosis. A summary of the investigated settings is presented in the bottom left panel. FSE, GRE, DESS, and FLAIR stand for fast spin echo, gradient echo, double-echo steady-state, and fluid-attenuated inversion recovery, respectively. We comprehensively investigate multiple CS-MRI tasks on a variety of common MRI settings with six datasets.

### B. Reconstruction-oriented co-design

The success of DL methods in CS-MRI reconstruction motivates the idea of jointly optimizing acquisition together with reconstruction via end-to-end training. Recently, there has been a rapidly growing literature on optimizing a parameterized sampling strategy jointly with a CNN reconstructor [9]–[23], [50]. These methods have different architectural designs and applicable scenarios, but all rely on the differentiable nature of neural networks to optimize the reconstruction accuracy over the choice of  $k$ -space measurements. The learned subsampling pattern and reconstruction network are thus specific to the dataset. The end-to-end training enables synergistic cooperation between the learned subsampling pattern and reconstructor, achieving state-of-the-art reconstruction performance. From a task perspective, however, having a reconstruction is not the end of the workflow. These methods rely on either human evaluation, a traditional task prediction algorithm, or a CNN for task predictions, which are out of the scope of these papers.

### C. Task-oriented co-design

Recent work has investigated the co-design idea in the context of limited tasks beyond full-FOV reconstruction, such as physical parameter estimation [50]–[52] and segmentation [53]–[56]. Using task-specific loss functions in their training procedures, these proposed methods demonstrate stronger task performance than methods trained by a reconstruction-only loss. Most of these proposed approaches leave either subsampling or prediction as a pre-determined fixed module, and focus on co-designing the other modules [50]–[54]. On the other hand, the authors of [55], [56] proposed methods for jointly optimizing all three steps, and investigated a brain segmentation task using a U-Net reconstructor and predictor. Although these methods show the potential of extending co-design beyond reconstruction, they are each fine-tuned for one particular

task, do not easily accommodate different types of data (e.g., multi-coil), and have not been demonstrated on real out-of-distribution datasets. In this work, we cast a wider net for the task-specific CS-MRI co-design problem. In particular we demonstrate our unified framework for designing generalized CS-MRI pipelines, TACKLE, on three different tasks beyond full FOV reconstruction. TACKLE performs robustly on this broad range of tasks and experiments, and is implemented and tested on a Siemens scanner.

## III. METHOD

Figure 2 illustrates the architecture of TACKLE. As a co-design CS-MRI method, TACKLE jointly optimizes the sampler, retriever, and predictor for a task-dependent loss. In the following subsections, we describe each module in order and more implementation details can be found in Supplement B.

### A. Sampler

We consider 2D Cartesian subsampling patterns, i.e.  $\mathbf{m} \in \{0, 1\}^n$ . We follow [9], [15], [57] to model the subsampling strategy as the element-wise Bernoulli distribution with a probability vector  $\mathbf{p} \in [0, 1]^n$ , i.e.  $\mathbf{m}_i \sim \text{Bern}(\mathbf{p}_i)$ . To learn the optimal sampling probabilities, we follow the sampler design of [9]. We optimize a set of parameters  $\mathbf{q}_i$  that first give us a set of probabilities  $\tilde{\mathbf{p}}_i := \text{Sigmoid}(\mathbf{q}_i)$ . We then rescale  $\tilde{\mathbf{p}}$  to obtain a probabilistic sampling mask  $\mathbf{p}$  that would result in  $b$  measurements in expectation via Bernoulli sampling:

$$\mathbf{p} = \begin{cases} \frac{\alpha}{\beta} \tilde{\mathbf{p}} & \text{if } \beta \geq \alpha \\ \mathbf{1} - \frac{1-\alpha}{1-\beta} (\mathbf{1} - \tilde{\mathbf{p}}) & \text{otherwise} \end{cases}$$

where  $\alpha := \frac{b}{n}$ ,  $\beta := \frac{\|\tilde{\mathbf{p}}\|_1}{n}$ , and  $\mathbf{1}$  is the all-one vector. During training, the sampler draws a  $k$ -space sampling mask  $\mathbf{m}$  by sampling  $\mathbf{m}_i \sim \text{Bern}(\mathbf{p}_i)$ . We repeatedly sample  $\mathbf{m}$  until  $\|\mathbf{m}\|_1 \approx b$  under a small tolerance. This sampling

process encourages exploration of different patterns and ensures the sampling patterns approximately satisfy the budget constraint. Since the sampling process is not differentiable, we use a straight-through estimator to overcome the non-differentiability [58]. During testing, we set the top  $b$  indices of  $\mathbf{p}$  with the highest probabilities to 1 (sample) and others to 0 (not sample). This binarization guarantees that the sampling mask strictly satisfies the sampling budget constraint and all slices of a volume share the same sampling mask. We also allocate  $1/8$  of the sampling budget for the low-frequency region around the DC component, which we refer to as the pre-select region. The pre-selected measurements provide auto-calibration signals (ACS) for multi-coil reconstruction and stabilize the training of some baselines. Therefore, we include the pre-select region for all experiments for consistency. More discussion on this can be found in Supplement B-C. We denote the sampler as  $S_q$  where  $\mathbf{q}$  is the vector of learnable parameters.

### B. Retriever

After acquiring measurements, we employ a retriever to extract visual information from noisy and subsampled  $k$ -space measurements. We note that we name the module “retriever” instead of “reconstructor” because it is jointly optimized with the downstream predictor for non-reconstruction tasks. Hence, the retriever should not be interpreted as a reconstructor as its output may not be a typical “reconstruction” in terms of point-wise accuracy. We denote the retriever as  $R_\theta$  where  $\theta$  is its weights. We select the E2E-VarNet [43] since it is a model-based DU architecture that combines forward model and learning prior, and achieves excellent performance on CS-MRI reconstruction [49]. E2E-VarNet also accommodates multi-coil  $k$ -space data with its ability to estimate coil sensitivity maps. Specifically, our E2E-VarNet retriever operates in  $k$ -space and consists of 12 refinement steps, each of which includes a U-Net [59] with independent weights from each other. For each U-Net, we use the standard architecture with the following parameters: 2 input and output channels, 18 channels after the first convolution filter, 4 average down-pooling layers, and 4 up-pooling layers. The final output layer of the retriever is an inverse Fourier transform followed by a root-sum-squares reduction for each pixel over all coils. The output of the retriever is a batch of single-channel images. For reconstruction tasks, a loss function will be directly applied to the output. For non-reconstruction tasks, the output will be fed into an additional predictor module described in the next section.

### C. Task-specific design: predictor and loss function

We demonstrate TACKLE on three tasks that together represent a gradual progression from generic full-FOV reconstruction to clinically relevant tasks.

1) *ROI-oriented reconstruction*: For many MRI scans, only a small region of the FOV is relevant to the reader, so we define a task where we aim to maximize reconstruction quality around that region. In contrast to the full-FOV reconstruction task, the reconstruction accuracy in this task is only measured over the region-of-interest (ROI) of each image instead of the entire FOV. We hereafter refer to this task as *ROI-oriented*

*reconstruction*. This task is a first step from generic full-FOV reconstruction to more specific downstream tasks in CS-MRI.

There is no predictor for this reconstruction task, and the output of the retriever will directly be used for evaluation. The evaluation metric we use is the local peak signal-to-noise ratio (PSNR), which is the PSNR within the ROI of an underlying image  $\mathbf{x}$ . Let  $\mathcal{R}_x$  be the set of indices  $i$  that are within the ROI of  $\mathbf{x}$ . Note that  $\mathcal{R}_x$  varies from one image  $\mathbf{x}$  to another. We define the local PSNR within the ROI as

$$\text{LocalPSNR}(\hat{\mathbf{x}}, \mathbf{x}; \mathcal{R}_x) := 10 \log_{10} \frac{\max(\mathbf{x})^2}{\text{LocalMSE}(\hat{\mathbf{x}}, \mathbf{x}; \mathcal{R}_x)} \quad (3)$$

where  $\text{LocalMSE}(\hat{\mathbf{x}}, \mathbf{x}; \mathcal{R}_x) := \frac{1}{|\mathcal{R}_x|} \sum_{i \in \mathcal{R}_x} (\hat{x}_i - x_i)^2$  and  $\max(\mathbf{x})$  is the largest pixel value of  $\mathbf{x}$ . We optimize our model for the local reconstruction quality using  $\mathcal{L}_{\text{ROI}}(\hat{\mathbf{x}}, \mathbf{x}) := -\text{LocalPSNR}(\hat{\mathbf{x}}, \mathbf{x}; \mathcal{R}_x)$  as the training loss.

2) *Tissue segmentation*: For this task, we aim to predict segmentation maps of different body tissues. Accurately segmenting a tissue from the rest of the organ provides important anatomical and pathological information [60]–[62]. Conventional segmentation workflow involves human evaluation and traditional algorithms, which often require standard reconstructions of certain contrasts as input [63]. On the contrary, TACKLE does not require reconstruction as a necessary intermediate step, and is optimized for segmentation performance in an end-to-end fashion.

We include an additional predictor  $P_\phi$  with weights  $\phi$  subsequent to the retriever. We choose the U-Net architecture due to its ability of solving medical image analysis tasks [59], [64], [65]. The specific parameters are: 1 input channel,  $c$  output channels (where  $c$  is the number of segmentation classes), 64 channels after the first convolution filter, 4 average down-pooling layers, and 4 up-pooling layers.

We use the Dice score [66]–[68] as the evaluation metric. The Dice score measures the degree of overlap between two segmentation maps and takes a value between 0 (no overlap) and 1 (perfect overlap). During training, we employ the Dice loss  $\mathcal{L}_{\text{seg}}(\hat{z}, z) := 1 - \text{DiceScore}(\hat{z}, z)$ . For both training and evaluation, we apply a Softmax function across all the classes for each pixel and then calculate the Dice loss/score. During the evaluation, we apply an additional binarization step where we set the class with highest value after Softmax as 1 and others as 0. In this way, we assign each pixel of the predicted segmentation map  $\hat{z}$  to exactly one class.

3) *Pathology classification*: The third task we consider is to determine whether a potential pathology exists in an MRI image, such as a suspected tumor. Using algorithms to automatically analyze MRI scans could lead to improved diagnosis accuracy in clinical practice [24]. We formulate this task as a binary image classification problem, where the negative class means the underlying image  $\mathbf{x}$  does not contain any pathology lesion and the positive class means it does contain a lesion. Through this proof-of-concept classification task, we go beyond pixel-level problems and show the benefit of task-specific co-design for solving an image-level problem.

Similar to the segmentation task, we include an additional predictor in the pipeline, which we also denote as  $P_\phi$  to



simplify notations. Specifically, we choose the ResNet [69], which is an established architecture for computer vision tasks, especially image classification. We use the standard ResNet18 architecture except for using 1 input channel and 2 output dimensions.

We use the binary cross entropy (BCE) as the loss function for this classification task,  $\mathcal{L}_{\text{class.}}(\hat{z}, z) := \text{BCE}(\hat{z}, z)$ . For evaluation metrics, we consider both the classification accuracy (ClsAcc :=  $\frac{\text{TP}+\text{TN}}{\text{TP}+\text{TN}+\text{FP}+\text{FN}}$ ) and the  $F_1$  score ( $F_1$  score :=  $\frac{2\text{TP}}{2\text{TP}+\text{FP}+\text{FN}}$ ) where TP, TN, FP, and FN are the number of True Positive, True Negative, False Positive, and False Negative, respectively. The classification accuracy is more interpretable, while the  $F_1$  score is more robust to class imbalance. So we include both metrics for a more comprehensive evaluation.

#### D. Training procedure

We summarize the training objective for each task as follows:

- ROI-oriented reconstruction:

$$\min_{q, \theta} \mathcal{L}_{\text{ROI}}(R_{\theta}(S_q \odot k), x)$$

- Segmentation or classification:

$$\min_{q, \theta, \phi} \mathcal{L}_{\text{seg./class.}}(P_{\phi}(R_{\theta}(S_q \odot k)), z)$$

where  $k \in \mathbb{C}^n$  contains all  $k$ -space measurements of  $x$ .

When performing end-to-end training over multiple stages, we empirically observed that a model trained from scratch tends to run into either optimization (hard to train) or generalization (unable to generalize) issues. Some prior works address these problems using a hybrid of reconstruction and task-dependent loss [51], [52], [54]–[56]. This approach requires tuning a weight parameter that balances the two losses. We adopt an alternative approach that avoids tuning this additional parameter. Specifically, we first train the sampler and retriever jointly with a full-FOV PSNR loss until convergence:

$$\min_{q, \theta} \mathcal{L}_{\text{FOV}}(R_{\theta}(S_q \odot k), x)$$

where  $\mathcal{L}_{\text{FOV}}(\hat{x}, x) := -\text{PSNR}(\hat{x}, x)$ . We refer to this as the pre-training step in later sections. With the weights learned for the sampler and retriever, we then add the predictor (initialized with random weights) into the framework and fine-tune all three components. We find that the pre-training step allows the model to better learn task-specific strategies, as demonstrated by an ablation study in Section VI-B. This training procedure mimics the training of foundation models in state-of-the-art language and vision models, which are first pre-trained on a general task and then fine-tuned for more specific tasks. Similar procedures can be found in other task-specific co-design papers, such as [53], [54].

## IV. EXPERIMENTS ON LARGE-SCALE DATASETS

We first demonstrate the effectiveness of our framework on the three considered tasks using large-scale datasets. We categorizes all the investigated datasets and settings in the bottom left panel of Figure 2. For each task, we demonstrate that the proposed task-specific co-design framework achieves

better performance than baselines that separately design reconstruction and prediction. We abbreviate different variants of the proposed method and baselines in the following way based on their task and training procedure:

Task	Training procedure and loss	Notation example
(ROI) recon.	S&R: PSNR loss S&R: local PSNR loss (w/ warm-up)	LP+UN <sub>FOV</sub> TACKLE <sub>ROI</sub>
Tissue seg.	S&R: PSNR loss → P: Dice loss S&R&P: Dice loss (w/ warm-up)	PD+UN <sub>recon.</sub> TACKLE <sub>seg.</sub>
Patho. class.	S&R: PSNR loss → P: BCE loss S&R&P: BCE loss (w/ warm-up)	LOUPE <sub>recon.</sub> TACKLE <sub>class.</sub>

S: sampler, R: retriever, P: predictor

→: separate training stages for reconstruction and prediction

To clarify, the subscript “recon.” for the segmentation and classification methods means that the sampler and retriever are trained for full-FOV reconstruction, and a predictor is subsequently trained for the downstream task with the sampler and retriever fixed. This is equivalent to training a predictor with the reconstructed images by these methods as input for the downstream task.

#### A. ROI-oriented reconstruction

**Dataset and setup** For the ROI-oriented reconstruction task, we use the images and raw single- and multi-coil  $k$ -space data from the fastMRI+ knee dataset [49], [70], which contains bounding box annotations for knee pathologies. Specifically, we investigate the most common knee pathology in the dataset called “Meniscus Tear” (MT). Each image  $x$  in the dataset contains at least one rectangular bounding box annotation  $\mathcal{R}_x$ , which is drawn to include all the pathology but exclude the normal surrounding anatomy [70]. Therefore the local image quality within each bounding box (i.e. ROI) is more indicative of the quality for pathology assessment than a metric over the entire FOV. We emphasize that the location of the bounding box  $\mathcal{R}_x$  varies sample by sample and is never an input to any method during inference.  $\mathcal{R}_x$  is only used for calculating the training loss and evaluating the local PSNR during test time according to (3). Hence, the local PSNR performance reflects the quality of reconstructions by different methods for assessing the considered pathological lesions in the ROIs.

**Baselines** We compare TACKLE<sub>ROI</sub> with three full-FOV reconstruction-oriented baselines.

- *LOUPE<sub>FOV</sub>*: Proposed in [9], LOUPE<sub>FOV</sub> jointly optimizes a sampler and a residual U-Net reconstructor.
- *Low-pass + U-Net<sub>FOV</sub> (LP+UN<sub>FOV</sub>)*: substitute the sampler in LOUPE<sub>FOV</sub> with a fixed low-pass filter sampling pattern.
- *Poisson-disc + U-Net<sub>FOV</sub> (PD+UN<sub>FOV</sub>)*: substitute the sampler in LOUPE<sub>FOV</sub> with a Poisson-disc sampling pattern drawn from a variable density distribution and generated with the `sigpy.mri.poisson` function in the `SigPy` package<sup>1</sup>.

**Results** We compare the average local PSNR of our method and other baselines over the test set in Table I. For all settings, TACKLE outperforms other baselines designed for full-FOV reconstruction by at least 3 dB, indicating a significant improvement of image quality within the ROI.

<sup>1</sup><https://github.com/mikgroup/sigpy>

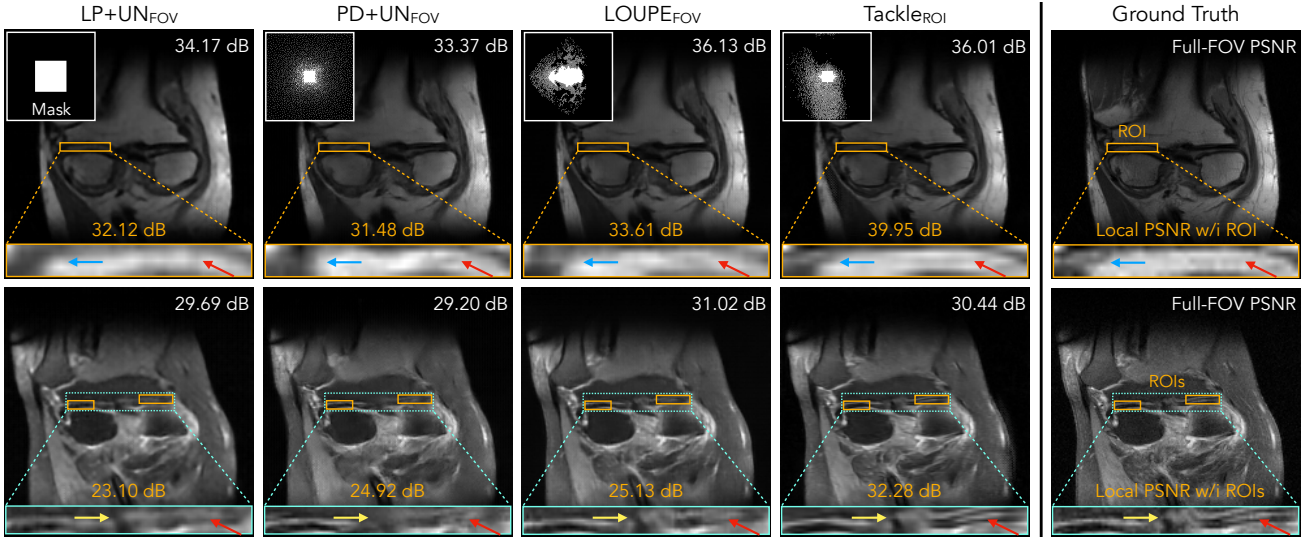


Fig. 3. Visual examples of two Meniscus Tear samples reconstructed by different methods in the  $16\times$  acceleration single-coil setting. For each reconstruction, the full-FOV PSNR is labeled in white, and the local PSNR for the ROI is in orange. Note how  $TACKLE_{ROI}$  recovers the structure and details of the ROI more accurately than the two baselines, as indicated by the red arrows. The better recovery of  $TACKLE_{ROI}$  over the ROI leads to a more accurate diagnosis of the Meniscus Tear. We emphasize that the location of the ROI is not an input to any of these models and is only used for evaluating the accuracy of each method on the region that contains the pathology.

TABLE I  
COMPARISON OF AVERAGE TEST LOCAL PEAK SIGNAL-TO-NOISE RATIO (LOCAL PSNR) IN DECIBEL (DB) WITHIN MENISCUS TEAR ROIS

Data	$R^*$	LP+UN <sub>FOV</sub>	PD+UN <sub>FOV</sub>	LOUPE <sub>FOV</sub>	TACKLE <sub>ROI</sub>
Single-coil	8	26.95	28.23	30.32	<b>34.04</b>
	16	25.16	26.05	27.32	<b>31.54</b>
Multi-coil	8	27.55	32.68	34.88	<b>40.65</b>
	16	26.02	30.00	31.79	<b>37.89</b>

\*  $R$ : acceleration ratio

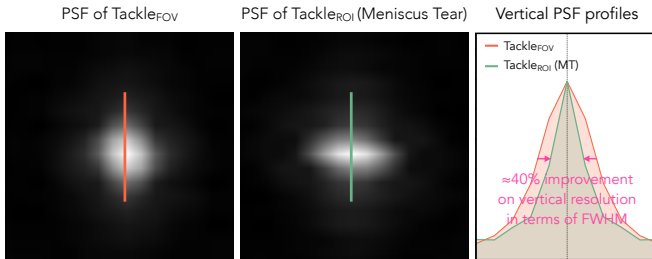


Fig. 4. Comparison of a subsampling PSF optimized for full-FOV reconstruction and another optimized for the reconstruction of meniscus tear (MT) ROIs. Optimizing for MT ROI reconstruction leads to around 40% improvement on the vertical resolution in terms of the *full width at half maximum* (FWHM), as shown by the PSF profiles in the bottom panel. This improved vertical resolution leads to a better reconstruction of the meniscus that has horizontal anatomy.

In Figure 3, we provide example reconstructions by our method and three baseline methods. For each reconstruction, its ROI is zoomed in on the bottom with the corresponding local PSNR value labeled above in orange. The full-FOV PSNR is labeled on the top right corner of each reconstruction. As shown in the ground truth of the MT example, a meniscus tear is indicated by a streak (dark in the top row and bright in the bottom row) that is present on the meniscus (bright in the top row and dark in the bottom row), as indicated by the red pointers. To accurately detect the existence and assess the severity of a meniscus tear, a reconstruction should clearly show

the boundaries of the meniscus and details of the tear. However, the ROIs of both LP+UN<sub>FOV</sub> and LOUPE<sub>FOV</sub> reconstructions contain significant reconstruction artifacts that disguise the tear (see the red arrows). On the other hand,  $TACKLE_{ROI}$  preserves the details of the tear and contains fewer artifacts than the baselines, providing a more accurate ROI reconstruction with a higher diagnostic value.

In Supplement D we also include an validation of  $TACKLE_{ROI}$  on images that either are healthy or contain pathologies other than the meniscus tear. Although  $TACKLE_{ROI}$  is not designed to generalize across different pathologies, we empirically find that  $TACKLE_{ROI}$  still yields high-fidelity reconstructions for out-of-distribution images so that the pathologies on these images remain detectable. This generalization of  $TACKLE_{ROI}$  is consistent across the three acceleration ratios ( $4\times$ ,  $8\times$ , and  $16\times$ ) for this fastMRI+ dataset.

**Discussion** Enhancing local ROIs for MRI may seem counter-intuitive, because the acquisition happens in  $k$ -space; each frequency measurement in theory corresponds to the entire FOV. Here we understand the feasibility via a PSF analysis. Consider the zero-filled reconstruction  $\tilde{x}$  from some (noiseless) single-coil  $k$ -space data:

$$\tilde{x} := F^{-1}(\mathbf{m} \odot (F\mathbf{x})) = (F^{-1}\mathbf{m}) * \mathbf{x}$$

where  $*$  denotes convolution and the second equality holds due to the Fourier convolution theorem. Here,  $F^{-1}\mathbf{m}$  is the PSF of the subsampling mask  $\mathbf{m}$  and determines the resolution of the CS-MRI system. We visualize the PSF of a sampling mask trained for full-FOV reconstruction and another trained for meniscus tear (MT) ROIs reconstruction with the same sampling budget in Figure 4. We plot the PSF profiles in the vertical direction around the main lobes. The PSF learned for MT ROIs reconstruction has around 40% improvement in vertical resolution in terms of *full width at half maximum* (FWHM) of the PSF profiles. Since MT ROIs contains the thin

TABLE II  
COMPARISON OF AVERAGE TEST DICE SCORE ON THE BRAIN SEGMENTATION TASK UNDER DIFFERENT ACCELERATION RATIOS ( $R$ )

$R$	PD+UN <sub>recon.</sub>	LOUPE <sub>recon.</sub>	SemuNet	TACKLE <sub>recon.</sub>	TACKLE <sub>seg.</sub>
16	0.8952	0.9244	0.9196	0.9350	<b>0.9395</b>
64	0.8377	0.8733	0.3824	0.9181	<b>0.9218</b>

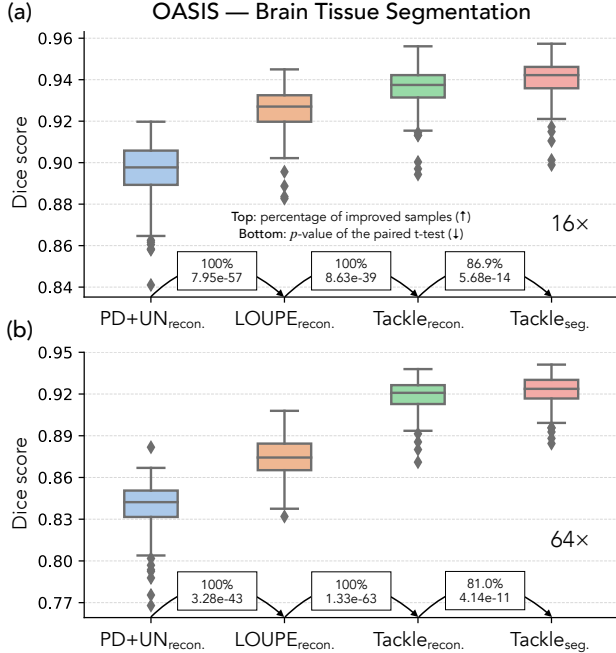


Fig. 5. Box plots of the brain tissue segmentation results under 16 $\times$  (a) and 64 $\times$  (b). For both acceleration ratios, TACKLE<sub>seg.</sub> outperforms other baselines in terms of all the statistical measures. Within the rectangle between each pair of methods in Figure 5, the top number is the percentage of improved samples and the bottom number is the  $p$ -value given by the paired samples t-test. A higher percentage and lower  $p$ -value indicate a more significant improvement.

horizontal anatomy of the meniscus, it makes sense that the learned subsampling pattern has a narrower PSF profile (and thus higher resolution) in the vertical direction. This comparison demonstrates that the improvement on ROIs is partly due to the capability of our model to optimize the subsampling PSF for local ROI anatomy via co-design. This is particularly beneficial when there is a mismatch between the optimal subsampling PSF for full-FOV reconstruction and that for ROI reconstruction due to directional anatomical structure, which is the case for MT ROI reconstruction.

### B. Tissue (brain) segmentation <sup>2</sup>

**Dataset and setup** This study involves segmenting four brain tissues: cortex, white matter, subcortical gray matter, and cerebrospinal fluid (CSF). Following [72], we use the 109-th coronal slice of each full  $k$ -space sampled volume in the OASIS dataset [73] and the segmentation maps generated with SAMSEG in FreeSurfer [63]. SAMSEG, which stands for Sequence Adaptive Multimodal SEGmentation, is an established method for brain tissue segmentation and is considered a standard method for this task [74]. We use the segmentation maps generated by SAMSEG as the supervised labels for

training. We simulate the single-coil  $k$ -space data for each image by taking the Fourier transform of the image and adding complex additive white Gaussian noise (AWGN), according to the forward model in (1). The standard deviation of the noise for each image is 0.05% of the magnitude of the DC component. We train each method to minimize the Dice loss until convergence and select the model with the highest Dice score on the validation set.

**Baselines** We compare TACKLE<sub>seg.</sub> with four baselines.

- **LOUPE<sub>recon.</sub>**: LOUPE<sub>recon.</sub> is a baseline based on LOUPE<sub>FOV</sub>. We first train a LOUPE<sub>FOV</sub> model for the full-FOV reconstruction task and then use the reconstructed images to separately train a segmentation network.
- **Poisson-disc + U-Net<sub>recon.</sub> (PD+UN<sub>recon.</sub>)**: same as LOUPE<sub>recon.</sub> except that the sampler is fixed to be a Poisson-disc sampling mask.
- **TACKLE<sub>recon.</sub>**: same as LOUPE<sub>recon.</sub> except for using the proposed architecture of TACKLE.
- **SemuNet**: Proposed in [56], SemuNet uses a hybrid of  $\ell_1$  reconstruction loss and cross-entropy segmentation loss.

**Results** We first provide a numerical comparison in Table II and a boxplot comparison in Figure 5. Within the rectangle between each pair of methods in Figure 5, the top number is the percentage of improved samples and the bottom number is the  $p$ -value given by the paired samples t-test. With an improved architecture, TACKLE<sub>recon.</sub> significantly outperforms the other reconstruction-oriented baselines. Nevertheless, TACKLE<sub>seg.</sub> still outperforms TACKLE<sub>recon.</sub> under both accelerations with significant  $p$ -values, highlighting the benefit of task-specific training. Compared to SemuNet [56], TACKLE<sub>seg.</sub> learns better segmentation strategies for both acceleration ratios and is more robust to high acceleration. We further provide some visual examples in Figure 6, visualizing the input and output of the predictor across different methods. The zoom-in regions highlight a location where the segmentation prediction of TACKLE<sub>seg.</sub> outperforms other baselines. Specifically, TACKLE<sub>seg.</sub> more accurately predicts the outline of the white matter (in yellow) than other methods. Such an improvement leads to more precise estimation of the thickness of the cortex (in orange), an important task for studying human cognition and neurodegeneration [71].

**Discussion** We note that TACKLE<sub>seg.</sub> learns an intermediate feature map as the input to the predictor, which circumvents a typically “good” reconstruction; it is interesting how the retriever produces an image where different brain tissues to be segmented have distinctive textures, which are easy to distinguish both from the background and from each other. Even though this feature map is not a typical “reconstruction” in terms of point-wise accuracy, it still accurately localizes the anatomy of the tissues to be segmented. We highlight that TACKLE<sub>recon.</sub> provides a high-fidelity reconstruction of the entire FOV with a PSNR of 36.77 dB, which demonstrates that our model is well capable of doing the reconstruction task accurately. However, TACKLE<sub>seg.</sub> still outperforms TACKLE<sub>recon.</sub> in terms of segmentation performance in Figure 6 and on average over the dataset in Table V (see Section VI-A for more details). This observation demonstrates that finding the most accurate full-FOV reconstruction does not necessarily lead to the optimal

<sup>2</sup>See knee segmentation results in Supplement A.

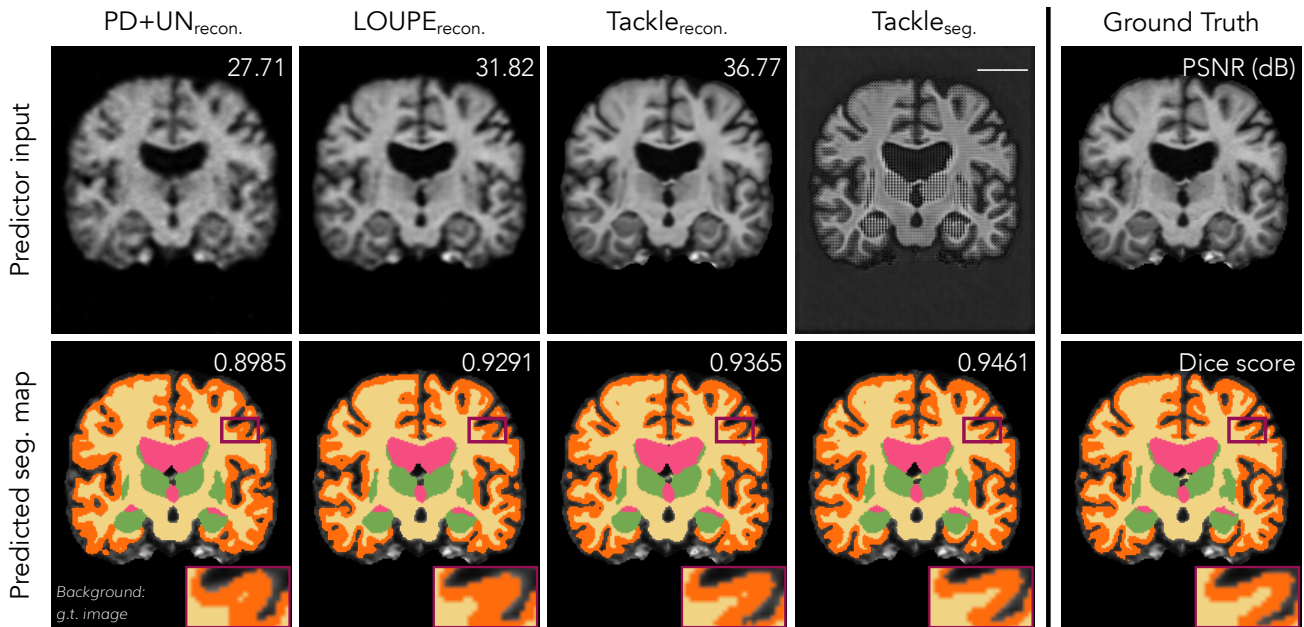


Fig. 6. Visual examples of two OASIS brain samples segmented by different methods in under  $16\times$  acceleration. We note that TACKLE<sub>seg.</sub> circumvents the typical “reconstruction” in terms of point-wise similarity with the ground truth image. Instead, it learns a feature map that accurately localizes the anatomy, leading to better segmentation prediction than other baselines both for this sample and on average over the test set (Table II). The zoom-in panels highlight a region where TACKLE<sub>seg.</sub> more accurately predicts the outline of white matter (in yellow) than other methods. This improvement leads to a more precise estimation of the thickness of the cortex (in orange), an important task for studying human cognition and neurodegeneration [71].

result on the considered segmentation task.

### C. Pathology (tumor) classification

**Dataset and setup** In this section, we demonstrate the effectiveness of the proposed method at detecting the existence of gliomas, a common type of brain tumors in adults. We use the images acquired by the FLAIR sequence in the Multimodal Brain Tumor Image Segmentation Benchmark (BRATS) dataset [24]. To obtain an image-level label of the existence of a tumor, we aggregate the pixel-level peritumoral edema (ED) segmentation annotations in the BRATS dataset by checking whether there exists any positive pixel in the segmentation map: negative (healthy) means there is no ED pixel, while positive (unhealthy) means there is at least one ED pixel. We use the same measurement simulation procedure as in Section IV-B. We train all models using the BCE loss and evaluate them using the classification accuracy and  $F_1$  score as described in Section III-C3. The  $k$ -space data is simulated in the same way as in Section IV-B.

**Baselines** We compare the proposed method TACKLE<sub>class.</sub> with the first three baselines as in Section IV-B except that the predictor of each baseline is subsequently trained for pathology classification rather than tissue segmentation (with input images optimized for full-FOV reconstruction). We do not include SemuNet here because it is originally proposed for the segmentation task only.

**Results** In Table III, we compare the classification-oriented method, TACKLE<sub>class.</sub>, with reconstruction-oriented baselines, and find that TACKLE<sub>class.</sub> achieves higher classification accuracy under both performance metrics. Specifically, TACKLE<sub>class.</sub> outperforms the existing reconstruction-oriented baseline LOUPE<sub>recon.</sub> by around 2% in the extreme  $64\times$

TABLE III  
COMPARISON OF AVERAGE TEST ACCURACY ON THE PATHOLOGY CLASSIFICATION TASK UNDER DIFFERENT ACCELERATION RATIOS ( $R$ )

Metric	$R$	PD+UN <sub>recon.</sub>	LOUPE <sub>recon.</sub>	TACKLE <sub>recon.</sub>	TACKLE <sub>class.</sub>
Cls. acc.	16	0.9016	0.9024	0.9062	<b>0.9159</b>
	64	0.8809	0.8930	0.9054	<b>0.9136</b>
$F_1$ score	16	0.8853	0.8846	0.8929	<b>0.9039</b>
	64	0.8628	0.8768	0.8910	<b>0.8992</b>

accelerated acquisition scenario. Both variants of TACKLE maintain competitive performance under the highly accelerated setting ( $R=64$ ), while PD+UN<sub>recon.</sub> and LOUPE<sub>recon.</sub> suffer from significant performance degradation. Note that TACKLE<sub>class.</sub> outperforms TACKLE<sub>recon.</sub> by more than 0.8% in both cases, despite having the same architecture. We also visualize and compare the classification performance of TACKLE<sub>class.</sub> and LOUPE<sub>recon.</sub> under  $16\times$  acceleration in Figure 7, using confusion matrices. The results show that TACKLE<sub>class.</sub> has substantially fewer false negatives (bottom left) and a higher overall accuracy compared to LOUPE<sub>recon.</sub>.

## V. VALIDATION ON AN EXPERIMENTALLY COLLECTED OUT-OF-DISTRIBUTION DATASET

In practice, creating a large well-annotated training set for a specific task can be very time-consuming or even infeasible. To demonstrate the immediate benefit of our method in a real-world setting, we conduct a validation of TACKLE on the ROI-oriented reconstruction task using experimentally collected data that is out of the distribution of the training data. Specifically, we train a TACKLE model on a large-scale dataset (fastMRI in this case) and directly test it on raw  $k$ -space data collected by *different hardware using a different type of sequence* from



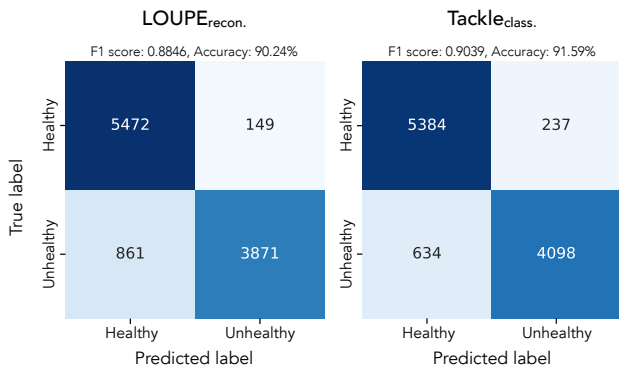


Fig. 7. Confusion matrices of the classification results by LOUPE<sub>recon.</sub> and TACKLE<sub>class.</sub>. Overall, TACKLE<sub>class.</sub> achieves greater accuracy in terms of both classification accuracy and  $F_1$  score than LOUPE<sub>recon.</sub>. TACKLE<sub>class.</sub> also has a significantly lower number of False Negatives (bottom left) compared to LOUPE<sub>recon.</sub>, which could lead to more patients receiving early treatment.

that of the training. Even without extra fine-tuning or test-time optimization, the learned ROI-specific model provides improved reconstructions on meniscus ROIs. In the following subsections, we present the details of this experiment.

**Data acquisition and processing** Two subjects were scanned at the Massachusetts General Hospital in accordance with institutional review board guidelines. Their right knees were scanned by a 3D-encoded Cartesian gradient-echo sequence with a 3 Tesla MRI scanner (Model: Skyra; Siemens Healthcare, Erlangen, Germany) and a single-channel extremity coil. To realize the 2D subsampling pattern in the coronal plane, we used a transversal orientation with the frequency encoding direction ( $k_x$ ) pointing into the knee cap (anterior-posterior), so that the two phase encoding directions were left-right ( $k_y$ ) and superior-inferior ( $k_z$ ), respectively. The acquisition parameters were as follows: TE/TR=4.8/9.1 ms, FOV=192×192×192 mm<sup>3</sup>, resolution=1×1×1 mm<sup>3</sup>, flip angle=10°. The total acquisition time of obtaining the fully sampled data for each subject was 5 minutes and 35 seconds. The raw  $k$ -space data had the shape of 192×192×192 ( $k_x \times k_y \times k_z$ ). We apply the 1D inverse Fourier transform along  $k_x$  for downstream processing. Specifically, we took the middle 40 slices of each volume and annotated bounding boxes around the meniscus region using an image labelling tool<sup>3</sup>. Efforts were made such that the locations and sizes of the bounding boxes roughly match those in the fastMRI MT dataset. We emphasize that these bounding boxes are *only* for the purpose of measuring the accuracy of different models on reconstructing the meniscus region. The locations of the annotated ROIs are *not* the input to any of the tested models.

**Generalization gaps** There are multiple generalization gaps between the training (fastMRI single-coil data) and test data:

- *Different hardware*: The acquired data are collected directly with a single-channel extremity coil, while the training data are simulated from  $k$ -space data collected by multi-channel receive coils [75].
- *Different sequence and resolution*: The acquired data are given by a gradient-echo sequence with 1 mm isotropic resolution, while the training data are given by a spin-echo sequence with 0.5 mm in-plane resolution [75].

<sup>3</sup><https://github.com/heartexlabs/labelImg>

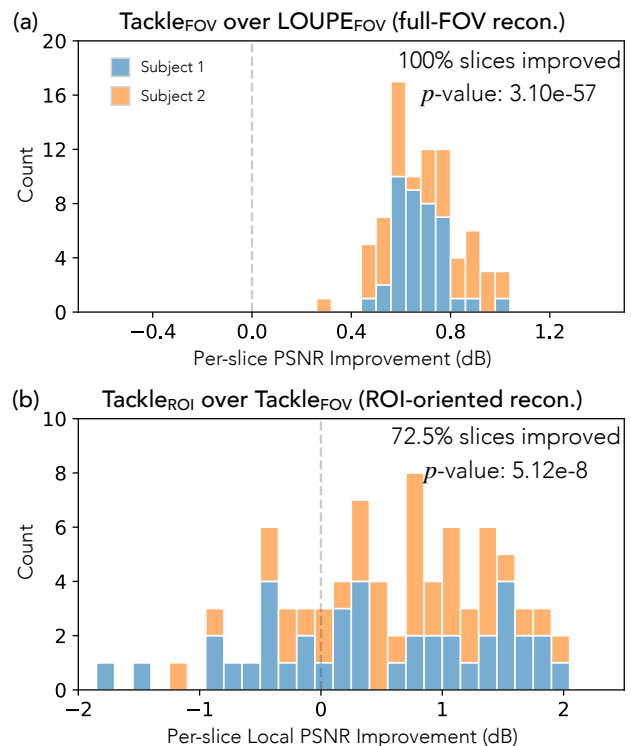


Fig. 8. Per-slice difference histograms. (a): TACKLE<sub>FOV</sub> over LOUPE<sub>FOV</sub> on the full-FOV reconstruction task and (b): TACKLE<sub>ROI</sub> over LOUPE<sub>FOV</sub> on the ROI-oriented reconstruction task. In both cases, the vast majority of slices improve and the  $p$ -values given by the paired samples t-test are highly significant.

- *Different distribution of the ROI anatomy*: The acquired data are collected from two subjects whose menisci are healthy and have no tear, while the ROIs in the training data contain meniscus tears.

Despite these generalization gaps, TACKLE<sub>ROI</sub> works robustly and leads to both numerical and visual improvement.

**Baselines** In this section, we compare TACKLE<sub>ROI</sub> with the following baselines under 4× acceleration.

- *Poisson-disc + Total Variation<sub>FOV</sub> (PD+TV<sub>FOV</sub>)*: The subsampling pattern is a Poisson-disc sampling mask generated with the `sigpy.mri.poisson` function in the `SigPy` package<sup>4</sup>. The reconstruction is obtained by solving a total variation (TV) regularized optimization problem with the Sparse MRI toolbox<sup>5</sup>.
- *LOUPE<sub>FOV</sub>*: the same LOUPE<sub>FOV</sub> baseline as in Section IV-A.
- *TACKLE<sub>FOV</sub>*: a TACKLE model trained for full-FOV reconstruction.
- *LOUPE<sub>ROI</sub>*: the same architecture as LOUPE<sub>FOV</sub> but trained for ROI reconstruction following the warm-up training procedure and using the local PSNR loss function.

**Results** We present a quantitative comparison in Table IV for both the full-FOV and ROI-oriented reconstruction tasks. For both tasks, TACKLE outperforms the baselines under the corresponding metric. For each task, we highlight the variant of TACKLE trained for the evaluation metric in green. Our

<sup>4</sup><https://github.com/mikgroup/sigpy>

<sup>5</sup><https://people.eecs.berkeley.edu/~mlustig/Software.html>

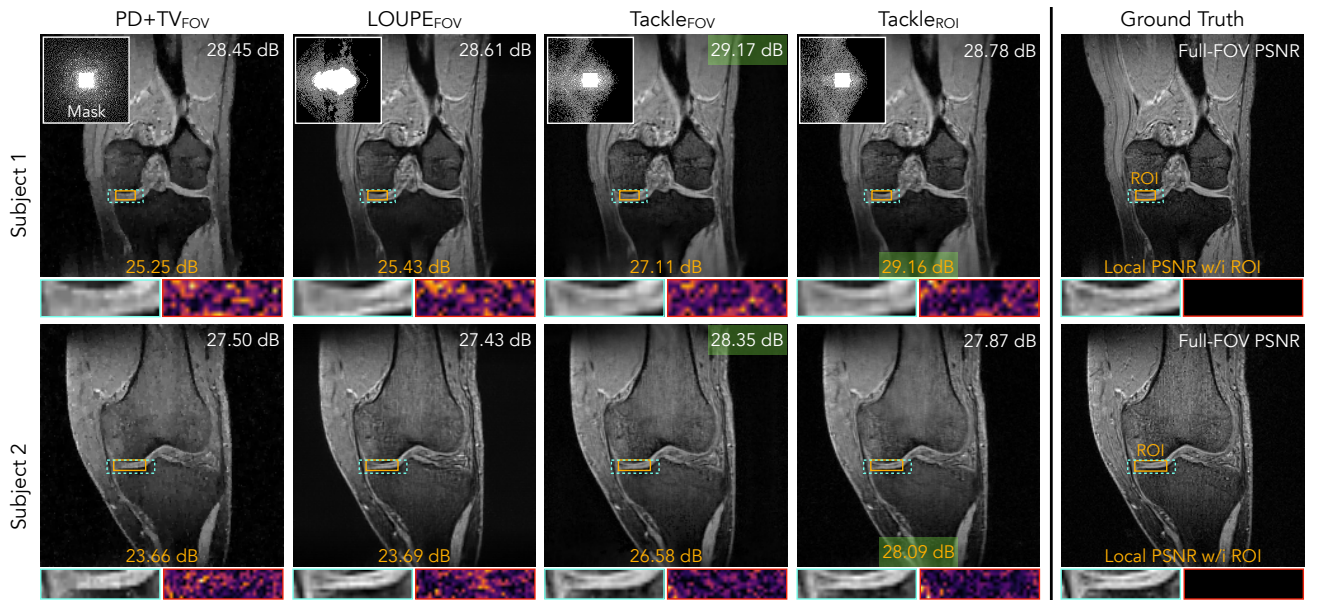


Fig. 9. Reconstruction comparison of two samples in the experimentally collected dataset (top: from subject 1; bottom: from subject 2) by different methods under  $4\times$  acceleration. The sampling mask, a zoom-in on the ROI, and the error map are presented for each method. By sampling more frequencies along the vertical direction in  $k$ -space, TACKLE<sub>ROI</sub> has a higher vertical resolution on the image space and thus outperforms other baselines optimized for full-FOV reconstruction on the ROIs with directional anatomical structure.

TABLE IV  
AVERAGE RECONSTRUCTION ACCURACY ON THE EXPERIMENTALLY COLLECTED DATASET UNDER  $4\times$  ACCELERATION  
(TOP: FULL-FOV RECON.; BOTTOM: ROI-ORIENTED RECON.)

Full-FOV recon.	PD+TV <sub>FOV</sub>	LOUPE <sub>FOV</sub>	TACKLE <sub>FOV</sub>	TACKLE <sub>ROI</sub>
PSNR (dB)	27.94	28.00	<b>28.70</b>	28.18
ROI recon.	PD+TV <sub>FOV</sub>	LOUPE <sub>FOV</sub>	TACKLE <sub>FOV</sub>	TACKLE <sub>ROI</sub>
Local PSNR (dB)	24.45	24.67	25.16	<b>25.72</b>

■ indicates the variant of TACKLE with matching training and evaluation metrics

results show that the highlighted variant outperforms the other variant of TACKLE, indicating a tradeoff between full-FOV and ROI reconstruction accuracy.

We further conduct a per-slice PSNR analysis in Figure 8. For both histograms, the horizontal axis is the improvement by the respective metric and the vertical axis is the count. We also quantify the significance of the improvements using the paired samples t-test. For the full-FOV reconstruction, TACKLE<sub>FOV</sub> outperforms LOUPE<sub>FOV</sub> on *all* 80 slices, giving a highly significant  $p$ -value of  $3.10e-57$ . We then compare TACKLE<sub>ROI</sub> with the better full-FOV reconstruction method, TACKLE<sub>FOV</sub>, on the ROI-oriented reconstruction task. Despite having the same architecture, TACKLE<sub>ROI</sub> still outperforms TACKLE<sub>FOV</sub> on 72.5% of slices, leading to a  $p$ -value of  $5.12e-8$ , which is also statistically significant. This result indicates that the ROI-oriented model TACKLE<sub>ROI</sub> indeed provides more accurate ROI reconstructions on this out-of-distribution dataset. We further provide some visual examples in Figure 9. Below each reconstruction is a zoom-in on the region around the ROI and the error map of the region with respect to the ground truth. TACKLE not only achieves higher PSNR values in both cases but also visually recovers the ROIs with fewer artifacts.

**Implementation** Besides the above results based on retro-

spective subsampling for quantitative comparison, we have also tested the learned sequence on a Siemens 3T MRI Skyra scanner. Specifically, we implement a re-ordering loop that iterates through all the trajectories based on our learned subsampling mask  $m$ . The implemented sequence *prospectively subsamples* in  $k$ -space and *shortens the scan time from 335 seconds to 84 seconds*, while maintaining the same level of visual quality on the ROI for which it is optimized. In Figure 10, we compare the reconstruction given by the prospectively subsampling sequence we implement with the reconstruction given by the retrospectively subsampled measurements from the fully sampling sequence. We note that the images labelled as “TACKLE<sub>ROI</sub> (retrospective)” and “TACKLE<sub>ROI</sub> (prospective)” are taken by two consecutive but separate scans, so there might be some subtle motion between them. Nevertheless, the two images have no significant visual difference, indicating that the improvement we show on retrospective simulations translates into actual improvement in practice. The prospective reconstruction successfully recovers important anatomical features around the meniscus region while only takes a quarter of the scan time compared to the full-sampled image.

## VI. ABLATION STUDIES

### A. Effectiveness of co-design

We evaluate the effectiveness of two aspects of co-design used in the proposed framework: learnable subsampling and task-specific training. In Table V, we compare four variants of the proposed method that have neither, one, and both aspects of co-design, respectively. The meanings of having or not having each aspect are summarized as follows:

- Learnable subsampling (column 2)
  - ✗ (*Poisson-disc*): use a Poisson-disc subsampling pattern that is randomly generated and then fixed
  - ✓: learn the subsampling pattern from data

TABLE V  
ABLATION STUDIES ON TWO ASPECTS OF CO-DESIGN FOR ALL THE CONSIDERED TASKS UNDER  $16\times$  ACCELERATION

Method	Ablated component		ROI-oriented reconstruction (Local PSNR in dB)		Tissue segmentation (Dice score)		Pathology classification (Cls. acc.) ( $F_1$ score)	
	Learned subsampling	Task-specific training	Single-coil	Multi-coil	Brain	Knee <sup>¶</sup>	Gliomas tumor	
							Cls. acc.	$F_1$ score
PD+VN <sub>b</sub>	✗ (Poisson-disc)	✗	29.91	36.48	0.9257	0.8018	0.9024	0.8871
PD+VN <sub>‡</sub>	✗ (Poisson-disc)	✓	30.15	36.51	0.9256	0.8474	0.9072	0.8966
TACKLE <sub>b</sub>	✓	✗	30.14	37.53	0.9350	0.8232	0.9062	0.8929
TACKLE <sub>‡</sub>	✓	✓	<b>31.54</b>	<b>37.89</b>	<b>0.9395</b>	<b>0.8532</b>	<b>0.9159</b>	<b>0.9039</b>

<sup>b</sup> indicates full-FOV reconstruction oriented versions of PD+VN and TACKLE

<sup>‡</sup> indicates task-specific versions of PD+VN and TACKLE

<sup>¶</sup> see Supplement A

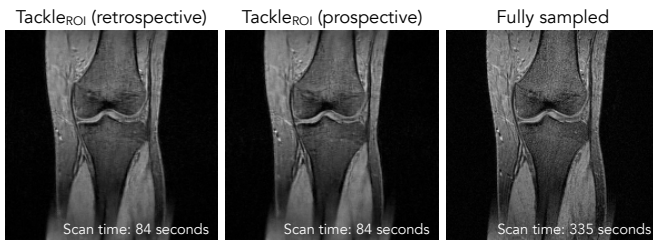


Fig. 10. Reconstruction comparison between the implemented prospective subsampling sequence with the retrospective subsampling sequence. The two reconstructions visually look the same, showing that our subsampling setup is realistic and does not generate significant artifacts on the reconstruction. Compared to the ground truth image, our prospectively subsampled reconstruction recovers important features around the meniscus region, which is the ROI it is trained to enhance.

- Task-specific training (column 3)
  - ✗: separately optimize retriever and predictor
  - ✓: jointly optimize retriever and predictor

To eliminate the effect of different network architectures, all four variants have the same retriever (E2E-VarNet) and predictor (U-Net for segmentation and ResNet for classification) architectures. Overall, we find both aspects of co-design are beneficial. For the task of reconstructing meniscus tear ROIs, learning the subsampling pattern is particularly helpful. Task-specific training, on the other hand, is more important for the knee segmentation task. Highlighted in cyan, the last row is the full-fledged version of TACKLE, which achieves the best performance for all considered scenarios with both aspects of co-design.

### B. Effectiveness of the proposed architecture and training procedure

The proposed architecture of  $\mathcal{T}_\theta$  from measurements  $\mathbf{y}$  to prediction  $\hat{\mathbf{z}}$  consists of an E2E-VarNet retriever and a U-Net predictor. A natural question is how this architecture compares with a single model-free neural network with a comparable number of parameters that directly maps subsampled measurements to the final prediction. We consider the following comparisons in Table VI:

- Single larger predictor (row 1)
  - *Tissue seg.*: U-Net with 128 channels after the first convolution layer and the same number of pooling layers (42.2M parameters)
  - *Patho. class.*: ResNet101 (42.5M parameters)
- VN+predictor (rows 2&3)
  - *Tissue seg.*: E2E-VarNet + standard U-Net (29.9M + 10.6M = 40.5M parameters)

TABLE VI  
ABLATION STUDIES ON MODEL ARCHITECTURE AND WARM-UP TRAINING FOR NON-RECONSTRUCTION TASKS UNDER  $16\times$  ACCELERATION

Ablated component		Tissue segmentation (Dice score)		Pathology classification (Cls. acc.)	
Arch. of $\mathcal{T}_\theta$	Pre-train	Brain	Knee <sup>¶</sup>	Gliomas tumor	
Predictor only <sup>‡</sup>	✗	0.9005	0.7539	0.8966	0.8788
VN+predictor <sup>‡</sup>	✗	0.9371	0.8163	0.9102	0.8969
VN+predictor <sup>§</sup>	✓	<b>0.9395</b>	<b>0.8532</b>	<b>0.9159</b>	<b>0.9039</b>

<sup>‡</sup> U-Net(128) / ResNet(101) for tissue seg. / patho. class.

<sup>§</sup> E2E-VarNet + U-Net(64) / ResNet(18) for tissue seg. / patho. class.

– *Patho. class.*: E2E-VarNet + ResNet18 (29.9M + 11.2M = 41.1M parameters)

Comparing the first two rows, we find that the proposed “VN+predictor” architecture significantly outperforms the “single larger predictor” baseline on all settings. This is likely due to the model-based nature of the “VN+predictor” architecture, which more effectively extracts useful information from subsampled measurements for downstream tasks. Finally, we include the pre-training step discussed in Section III-D. Highlighted in cyan, the full-fledged version of TACKLE in the last row significantly outperforms the ablated baselines on both non-reconstruction tasks, indicating the importance of both the proposed architecture and training procedure.

## VII. CONCLUSION

In this work, we generalized the objective of CS-MRI co-design to a variety of tasks beyond full-FOV reconstruction. We introduced TACKLE as a unified approach for robustly learning task-specific strategies. Through comprehensive experiments, we showed that TACKLE outperforms existing DL techniques that separately learn subsampling pattern, reconstruction, and prediction. Additionally, TACKLE outperforms naive attempts for co-design that attempt to learn a direct mapping from measurements to predictions. We found that the optimized strategies sometimes circumvents the typical reconstruction in terms of point-wise accuracy, but effectively extracts key visual information useful for task prediction. Through ablation studies, we justify multiple design choices with regard to architecture and training procedure, and show their importance in effectively learning CS-MRI strategies for tasks that go beyond full-FOV reconstruction. We further implemented a learned subsampling sequence and tested it on a Siemens 3T MRI Skyra scanner, which leads to a four-fold scan time reduction without sacrificing visual quality. Our study demonstrates the exciting promise of employing end-to-end co-design techniques, suggesting a future where clinical CS-MRI

requirements are addressed with enhanced efficiency while maintaining accuracy.

#### ACKNOWLEDGMENTS

This work was sponsored by NSF Award 2048237, NIH Projects 5R01AG064027, 5R01AG070988, R21EB029641, R01HD099846, R01HD085813, Heritage Medical Research Fellowship, S2I Clinard Innovation Award, and Rockley Photonics. Z.W. was sponsored by the Kortschak Fellowship, Amazon AI4Science Fellowship, and Amazon AI4Science Partnership Discovery Grant.

#### REFERENCES

- [1] M. Lustig, D. Donoho, and J. Pauly, "Sparse MRI: The application of compressed sensing for rapid MR imaging," *Magnetic resonance in medicine : official journal of the Society of Magnetic Resonance in Medicine / Society of Magnetic Resonance in Medicine*, vol. 58, pp. 1182–95, 12 2007.
- [2] M. Lustig, D. L. Donoho, J. M. Santos, and J. M. Pauly, "Compressed sensing MRI," *IEEE Signal Processing Magazine*, vol. 25, no. 2, pp. 72–82, 2008.
- [3] Y. Romano, M. Elad, and P. Milanfar, "The little engine that could: Regularization by denoising (RED)," *SIAM Journal on Imaging Sciences*, vol. 10, 11 2016.
- [4] R. Ahmad, C. Bouman, G. Buzzard, S. Chan, S. Liu, E. Reehorst, and P. Schniter, "Plug-and-play methods for magnetic resonance imaging: Using denoisers for image recovery," *IEEE Signal Processing Magazine*, vol. 37, pp. 105–116, 01 2020.
- [5] J. Liu, Y. Sun, C. Eldeniz, W. Gan, H. An, and U. S. Kamilov, "RARE: image reconstruction using deep priors learned without groundtruth," *IEEE J. Sel. Top. Signal Process.*, vol. 14, no. 6, pp. 1088–1099, 2020.
- [6] Y. Yang, J. Sun, H. Li, and Z. Xu, "Deep ADMM-Net for compressive sensing MRI," in *Advances in Neural Information Processing Systems 29: Annual Conference on Neural Information Processing Systems 2016, December 5-10, 2016, Barcelona, Spain*, 2016, pp. 10–18.
- [7] J. Schlemper, J. Caballero, J. V. Hajnal, A. N. Price, and D. Rueckert, "A deep cascade of convolutional neural networks for dynamic MR image reconstruction," *IEEE Trans. Medical Imaging*, vol. 37, no. 2, pp. 491–503, 2018.
- [8] J. Zhang and B. Ghanem, "ISTA-Net: Interpretable optimization-inspired deep network for image compressive sensing," 06 2018, pp. 1828–1837.
- [9] C. D. Bahadir, A. V. Dalca, and M. R. Sabuncu, "Learning-based optimization of the under-sampling pattern in MRI," in *International Conference on Information Processing in Medical Imaging*. Springer, 2019, pp. 780–792.
- [10] Z. Zhang, A. Romero, M. J. Muckley, P. Vincent, L. Yang, and M. Drozdal, "Reducing uncertainty in undersampled MRI reconstruction with active acquisition," in *Proceedings of the IEEE Conference on Computer Vision and Pattern Recognition*, 2019, pp. 2049–2058.
- [11] J. Zhang, H. Zhang, A. Wang, Q. Zhang, M. R. Sabuncu, P. Spincemaille, T. D. Nguyen, and Y. Wang, "Extending LOUPE for k-space under-sampling pattern optimization in multi-coil MRI," in *Machine Learning for Medical Image Reconstruction - Third International Workshop, MLMIR 2020, Held in Conjunction with MICCAI 2020, Lima, Peru, October 8, 2020, Proceedings*, ser. Lecture Notes in Computer Science, vol. 12450. Springer, 2020, pp. 91–101.
- [12] H. K. Aggarwal and M. Jacob, "J-ModL: Joint model-based deep learning for optimized sampling and reconstruction," *IEEE Journal of Selected Topics in Signal Processing*, vol. 14, no. 6, pp. 1151–1162, 2020.
- [13] C. Alkan, M. Mardani, S. Vasanawala, and J. M. Pauly, "Learning to sample MRI via variational information maximization," in *NeurIPS 2020 Workshop on Deep Learning and Inverse Problems*, 2020. [Online]. Available: [https://openreview.net/forum?id=1AOReNkDmh\\_](https://openreview.net/forum?id=1AOReNkDmh_)
- [14] G. Wang, T. Luo, J.-F. Nielsen, D. C. Noll, and J. A. Fessler, "B-Spline parameterized joint optimization of reconstruction and k-space trajectories (BJORK) for accelerated 2d MRI," 2021.
- [15] S. Xue, Z. Cheng, G. Han, C. Sun, K. Fang, Y. Liu, J. Cheng, X. Jin, and R. Bai, "2D probabilistic undersampling pattern optimization for MR image reconstruction," *Medical Image Analysis*, vol. 77, p. 102346, 2022. [Online]. Available: <https://www.sciencedirect.com/science/article/pii/S1361841521003911>
- [16] W. Peng, L. Feng, G. Zhao, and F. Liu, "Learning optimal k-space acquisition and reconstruction using physics-informed neural networks," in *Proceedings of the IEEE/CVF Conference on Computer Vision and Pattern Recognition (CVPR)*, June 2022, pp. 20794–20803.
- [17] G. Wang, J.-F. Nielsen, J. A. Fessler, and D. C. Noll, "Stochastic optimization of 3D non-cartesian sampling trajectory (SNOPY)," *arXiv preprint arXiv:2209.11030*, 2022.
- [18] J. Yang, X.-X. Li, F. Liu, D. Nie, P. Lio, H. Qi, and D. Shen, "Fast multi-contrast MRI acquisition by optimal sampling of information complementary to pre-acquired MRI contrast," *IEEE Transactions on Medical Imaging*, pp. 1–1, 2022.
- [19] F. Martinini, M. Mangia, A. Marchioni, R. Rovatti, and G. Setti, "A deep learning method for optimal undersampling patterns and image recovery for MRI exploiting losses and projections," *IEEE Journal of Selected Topics in Signal Processing*, vol. 16, no. 4, pp. 713–724, 2022.
- [20] J. Wang, Q. Yang, Q. Yang, L. Xu, C. Cai, and S. Cai, "Joint optimization of cartesian sampling patterns and reconstruction for single-contrast and multi-contrast fast magnetic resonance imaging," *Computer Methods and Programs in Biomedicine*, vol. 226, p. 107150, 2022. [Online]. Available: <https://www.sciencedirect.com/science/article/pii/S0169260722005314>
- [21] Z. Wang, B. Li, W. Xia, C. Shen, M. Hou, H. Chen, Y. Liu, J. Zhou, and Y. Zhang, "Leaders: Learnable deep radial subsampling for MRI reconstruction," in *2022 IEEE 19th International Symposium on Biomedical Imaging (ISBI)*. IEEE, 2022, pp. 1–5.
- [22] G. Chaitnya, Z. Ramzi, and P. Ciuciu, "Hybrid learning of non-cartesian k-space trajectory and MR image reconstruction networks," in *2022 IEEE 19th International Symposium on Biomedical Imaging (ISBI)*. IEEE, 2022, pp. 1–5.
- [23] M. V. W. Zibetti, F. Knoll, and R. R. Regatte, "Alternating learning approach for variational networks and undersampling pattern in parallel MRI applications," *IEEE Transactions on Computational Imaging*, vol. 8, pp. 449–461, 2022.
- [24] B. Menze, A. Jakab, S. Bauer, J. Kalpathy-Cramer, K. Farahaniy, J. Kirby, Y. Burren, N. Porz, J. Slotboom, R. Wiest, L. Lancziy, E. Gerstner, M.-A. Webery, T. Arbel, B. Avants, N. Ayache, P. Buendia, L. Collins, N. Cordier, and K. Van Leemput, "The multimodal brain tumor image segmentation benchmark (BRATS)," *IEEE Transactions on Medical Imaging*, vol. 99, 12 2014.
- [25] E. J. Candès, J. K. Romberg, and T. Tao, "Robust uncertainty principles: exact signal reconstruction from highly incomplete frequency information," *IEEE Trans. Inf. Theory*, vol. 52, no. 2, pp. 489–509, 2006.
- [26] A. Danielyan, V. Katkovnik, and K. Egiazarian, "BM3D frames and variational image deblurring," *IEEE transactions on image processing : a publication of the IEEE Signal Processing Society*, vol. 21, 06 2011.
- [27] M. Elad and M. Aharon, "Image denoising via sparse and redundant representations over learned dictionaries," *IEEE transactions on image processing : a publication of the IEEE Signal Processing Society*, vol. 15, pp. 3736–45, 01 2007.
- [28] L. Rudin, S. Osher, and E. Fatemi, "Nonlinear total variation based noise removal algorithms," *Physica D: Nonlinear Phenomena*, vol. 60, pp. 259–268, 11 1992.
- [29] H. Wang, D. Liang, and L. Ying, "Pseudo 2D random sampling for compressed sensing MRI," *2009 Annual International Conference of the IEEE Engineering in Medicine and Biology Society*, pp. 2672–2675, 2009.
- [30] S. Vasanawala, M. Murphy, M. Alley, P. Lai, K. Keutzer, J. Pauly, and M. Lustig, "Practical parallel imaging compressed sensing MRI: Summary of two years of experience in accelerating body MRI of pediatric patients," in *2011 IEEE International Symposium on Biomedical Imaging: From Nano to Macro*, 2011, pp. 1039–1043.
- [31] N. Chauffert, P. Ciuciu, J. Kahn, and P. Weiss, "Variable density sampling with continuous trajectories," *SIAM Journal on Imaging Sciences*, vol. 7, no. 4, pp. 1962–1992, 2014.
- [32] R. L. Cook, "Stochastic sampling in computer graphics," vol. 5, no. 1, p. 51–72, jan 1986. [Online]. Available: <https://doi.org/10.1145/7529.8927>
- [33] R. Raja and N. Sinha, "Adaptive k-space sampling design for edge-enhanced DCE-MRI using compressed sensing," *Magnetic Resonance Imaging*, vol. 32, 09 2014.
- [34] S. Venkatakrishnan, C. Bouman, and B. Wohlberg, "Plug-and-play priors for model based reconstruction," 12 2013, pp. 945–948.
- [35] U. S. Kamilov, C. A. Bouman, G. T. Buzzard, and B. Wohlberg, "Plug-and-play methods for integrating physical and learned models in computational imaging," 2022. [Online]. Available: <https://arxiv.org/abs/2203.17061>
- [36] S. Wang, Z. Su, L. Ying, X. Peng, S. Zhu, F. Liang, D. Feng, and D. Liang, "Accelerating magnetic resonance imaging via deep learning," in *13th IEEE International Symposium on Biomedical Imaging, ISBI*



- 2016, Prague, Czech Republic, April 13-16, 2016. IEEE, 2016, pp. 514–517.
- [37] D. Lee, J. J. Yoo, and J. C. Ye, “Deep residual learning for compressed sensing MRI,” in *14th IEEE International Symposium on Biomedical Imaging, ISBI 2017, Melbourne, Australia, April 18-21, 2017*. IEEE, 2017, pp. 15–18.
- [38] D. Lee, J. Yoo, S. Tak, and J. C. Ye, “Deep residual learning for accelerated MRI using magnitude and phase networks,” *IEEE Transactions on Biomedical Engineering*, vol. 65, no. 9, pp. 1985–1995, 2018.
- [39] G. Yang, S. Yu, H. Dong, G. Slabaugh, P. Dragotti, X. Ye, F. Liu, S. Arridge, J. Keegan, Y. Guo, and D. Firmin, “DAGAN: Deep de-aliasing generative adversarial networks for fast compressed sensing MRI reconstruction,” *IEEE Transactions on Medical Imaging*, vol. PP, pp. 1–1, 12 2017.
- [40] T. M. Quan, T. Nguyen-Duc, and W.-K. Jeong, “Compressed sensing MRI reconstruction with cyclic loss in generative adversarial networks,” *IEEE Transactions on Medical Imaging*, vol. PP, 09 2017.
- [41] K. Hammernik, T. Klatzer, E. Kobler, M. Recht, D. Sodickson, T. Pock, and F. Knoll, “Learning a variational network for reconstruction of accelerated MRI data,” *Magnetic Resonance in Medicine*, vol. 79, 04 2017.
- [42] H. K. Aggarwal, M. P. Mani, and M. Jacob, “MoDL: Model-based deep learning architecture for inverse problems,” *IEEE Transactions on Medical Imaging*, vol. 38, no. 2, pp. 394–405, 2019.
- [43] A. Sriram, J. Zbontar, T. Murrell, A. Defazio, C. L. Zitnick, N. Yakubova, F. Knoll, and P. Johnson, “End-to-end variational networks for accelerated MRI reconstruction,” in *International Conference on Medical Image Computing and Computer-Assisted Intervention*. Springer, 2020, pp. 64–73.
- [44] S. A. H. Hosseini, B. Yaman, S. Moeller, M. Hong, and M. Akçakaya, “Dense recurrent neural networks for accelerated MRI: History-cognizant unrolling of optimization algorithms,” *IEEE Journal of Selected Topics in Signal Processing*, vol. PP, pp. 1–1, 06 2020.
- [45] J. Liu, Y. Sun, W. Gan, X. Xu, B. Wohlberg, and U. S. Kamilov, “SGD-Net: Efficient model-based deep learning with theoretical guarantees,” *CoRR*, vol. abs/2101.09379, 2021.
- [46] J. Adler and O. Ozan, “Learned primal-dual reconstruction,” *IEEE Transactions on Medical Imaging*, vol. PP, 07 2017.
- [47] B. Yaman, S. A. H. Hosseini, S. Moeller, J. Ellermann, K. Uğurbil, and M. Akçakaya, “Self-supervised learning of physics-guided reconstruction neural networks without fully sampled reference data,” *Magnetic resonance in medicine*, vol. 84, 07 2020.
- [48] D. Gilton, G. Ongie, and R. Willett, “Deep equilibrium architectures for inverse problems in imaging,” *IEEE Transactions on Computational Imaging*, vol. 7, pp. 1123–1133, 2021.
- [49] J. Zbontar, F. Knoll, A. Sriram, M. J. Muckley, M. Bruno, A. Defazio, M. Parente, K. J. Geras, J. Katsnelson, H. Chandarana, Z. Zhang, M. Drozdal, A. Romero, M. Rabbat, P. Vincent, J. Pinkerton, D. Wang, N. Yakubova, E. Owens, C. L. Zitnick, M. P. Recht, D. K. Sodickson, and Y. W. Lui, “fastMRI: An open dataset and benchmarks for accelerated MRI,” 2018.
- [50] L. Zhao, X. Chen, E. Z. Chen, Y. Liu, D. Shen, T. Chen, and S. Sun, “JoJoNet: Joint-contrast and joint-sampling-and-reconstruction network for multi-contrast MRI,” *arXiv preprint arXiv:2210.12548*, 2022.
- [51] J. Zou and Y. Cao, “Joint optimization of k-t sampling pattern and reconstruction of DCE MRI for pharmacokinetic parameter estimation,” *IEEE Transactions on Medical Imaging*, vol. 41, no. 11, pp. 3320–3331, 2022.
- [52] X. Xu, W. Gan, S. Kothapalli, D. Yablonskiy, and U. Kamilov, “CoRECT: A deep unfolding framework for motion-corrected quantitative R2\* mapping,” 10 2022.
- [53] Z. Fan, L. Sun, X. Ding, Y. Huang, C. Cai, and J. Paisley, “A segmentation-aware deep fusion network for compressed sensing MRI,” in *Computer Vision – ECCV 2018: 15th European Conference, Munich, Germany, September 8–14, 2018, Proceedings, Part VI*, 2018, p. 55–70.
- [54] L. Sun, Z. Fan, Y. Huang, X. Ding, and J. W. Paisley, “Joint CS-MRI reconstruction and segmentation with a unified deep network,” in *Information Processing in Medical Imaging*, 2018.
- [55] T. Weiss, O. Senouf, S. Vedula, O. Michailovich, M. Zibulevsky, and A. Bronstein, “PILOT: Physics-informed learned optimized trajectories for accelerated MRI,” 2020.
- [56] Z. Wang, W. Xia, Z. Lu, Y. Huang, Y. Liu, H. Chen, J. Zhou, and Y. Zhang, “One network to solve them all: A sequential multi-task joint learning network framework for MR imaging pipeline,” in *Machine Learning for Medical Image Reconstruction: 4th International Workshop, MLMIR 2021, Held in Conjunction with MICCAI 2021, Strasbourg, France, October 1, 2021, Proceedings*, 2021, p. 76–85. [Online]. Available: [https://doi.org/10.1007/978-3-030-88552-6\\_8](https://doi.org/10.1007/978-3-030-88552-6_8)
- [57] T. Yin, Z. Wu, H. Sun, A. V. Dalca, Y. Yue, and K. L. Bouman, “End-to-end sequential sampling and reconstruction for MRI,” in *Proceedings of Machine Learning for Health*, ser. Proceedings of Machine Learning Research, S. Roy, S. Pfohl, E. Rocheteau, G. A. Tadesse, L. Oala, F. Falck, Y. Zhou, L. Shen, G. Zamzmi, P. Mugambi, A. Zirikly, M. B. A. McDermott, and E. Alsentzer, Eds., vol. 158. PMLR, 04 Dec 2021, pp. 261–281. [Online]. Available: <https://proceedings.mlr.press/v158/yin21a.html>
- [58] Y. Bengio, N. Léonard, and A. Courville, “Estimating or propagating gradients through stochastic neurons for conditional computation,” *arXiv preprint arXiv:1308.3432*, 2013.
- [59] O. Ronneberger, P. Fischer, and T. Brox, “U-Net: Convolutional networks for biomedical image segmentation,” in *International Conference on Medical Image Computing and Computer-Assisted Intervention*. Springer, 2015, pp. 234–241.
- [60] T. Heimann, B. J. Morrison, M. A. Styner, M. Niethammer, and S. Warfield, “Segmentation of knee images: a grand challenge,” in *Proc. MICCAI Workshop on Medical Image Analysis for the Clinic*. Beijing, China, 2010, pp. 207–214.
- [61] F. Schick, “Tissue segmentation: a crucial tool for quantitative MRI and visualization of anatomical structures,” *Magma (New York, N.Y.)*, vol. 29, 04 2016.
- [62] A. Raj, S. Vishwanathan, B. Ajani, K. Krishnan, and H. Agarwal, “Automatic knee cartilage segmentation using fully volumetric convolutional neural networks for evaluation of osteoarthritis,” in *2018 IEEE 15th International Symposium on Biomedical Imaging (ISBI 2018)*. IEEE, 2018, pp. 851–854.
- [63] B. Fischl, “Freesurfer,” *NeuroImage*, vol. 62, pp. 774–81, 01 2012.
- [64] G. Balakrishnan, A. Zhao, M. R. Sabuncu, J. Guttag, and A. V. Dalca, “VoxelMorph: a learning framework for deformable medical image registration,” *IEEE transactions on medical imaging*, vol. 38, no. 8, pp. 1788–1800, 2019.
- [65] V. Ghodrati, J. Shao, M. Bydder, Z. Zhou, W. Yin, K.-L. Nguyen, Y. Yang, and P. Hu, “MR image reconstruction using deep learning: evaluation of network structure and loss functions,” *Quantitative imaging in medicine and surgery*, vol. 9, no. 9, p. 1516, 2019.
- [66] L. R. Dice, “Measures of the amount of ecologic association between species,” *Ecology*, vol. 26, no. 3, pp. 297–302, 1945. [Online]. Available: <http://www.jstor.org/stable/1932409>
- [67] K. H. Zou, S. K. Warfield, A. Bharatha, C. M. C. Tempany, M. R. Kaus, S. J. Haker, r. Wells, William M, F. A. Jolesz, and R. Kikinis, “Statistical validation of image segmentation quality based on a spatial overlap index,” *Academic radiology*, vol. 11, no. 2, pp. 178–189, 02 2004. [Online]. Available: <https://pubmed.ncbi.nlm.nih.gov/14974593>
- [68] F. Milletari, N. Navab, and S.-A. Ahmadi, “V-Net: Fully convolutional neural networks for volumetric medical image segmentation,” in *2016 fourth international conference on 3D vision (3DV)*. IEEE, 2016, pp. 565–571.
- [69] K. He, X. Zhang, S. Ren, and J. Sun, “Deep residual learning for image recognition,” in *Proceedings of the IEEE conference on computer vision and pattern recognition*, 2016, pp. 770–778.
- [70] R. Zhao, B. Yaman, Y. Zhang, R. Stewart, A. Dixon, F. Knoll, Z. Huang, Y. W. Lui, M. S. Hansen, and M. P. Lungren, “fastMRI+, clinical pathology annotations for knee and brain fully sampled magnetic resonance imaging data,” *Scientific Data*, vol. 9, no. 1, p. 152, 2022. [Online]. Available: <https://doi.org/10.1038/s41597-022-01255-z>
- [71] L. Apostolova and P. Thompson, “Brain mapping as a tool to study neurodegeneration,” *Neurotherapeutics: the journal of the American Society for Experimental NeuroTherapeutics*, vol. 4, pp. 387–400, 08 2007.
- [72] A. Hoopes, M. Hoffmann, B. Fischl, J. Guttag, and A. V. Dalca, “HyperMorph: Amortized hyperparameter learning for image registration,” in *Information Processing in Medical Imaging: 27th International Conference, IPMI 2021, Virtual Event, June 28–June 30, 2021, Proceedings*. Berlin, Heidelberg: Springer-Verlag, 2021, p. 3–17. [Online]. Available: [https://doi.org/10.1007/978-3-030-78191-0\\_1](https://doi.org/10.1007/978-3-030-78191-0_1)
- [73] D. Marcus, T. Wang, J. Parker, J. Csernansky, J. Morris, and R. Buckner, “Open access series of imaging studies (OASIS): Cross-sectional MRI data in young, middle aged, nondemented, and demented older adults,” *Journal of cognitive neuroscience*, vol. 19, pp. 1498–507, 10 2007.
- [74] O. Puonti, J. Iglesias, and K. Van Leemput, “Fast and sequence-adaptive whole-brain segmentation using parametric bayesian modeling,” *NeuroImage*, vol. 143, 09 2016.
- [75] F. Knoll, J. Zbontar, A. Sriram, M. J. Muckley, M. Bruno, A. Defazio, M. Parente, K. J. Geras, J. Katsnelson, H. Chandarana, Z. Zhang,

- M. Drozdal, A. Romero, M. Rabbat, P. Vincent, J. Pinkerton, D. Wang, N. Yakubova, E. Owens, C. L. Zitnick, M. P. Recht, D. K. Sodickson, and Y. W. Lui, “fastMRI: A publicly available raw k-space and dicom dataset of knee images for accelerated MR image reconstruction using machine learning,” *Radiology: Artificial Intelligence*, vol. 2, no. 1, p. e190007, 2020, pMID: 32076662. [Online]. Available: <https://doi.org/10.1148/ryai.2020190007>
- [76] A. D. Desai, A. M. Schmidt, E. B. Rubin, C. M. Sandino, M. S. Black, V. Mazzoli, K. J. Stevens, R. Boutin, C. Re, G. E. Gold, B. Hargreaves, and A. Chaudhari, “SKM-TEA: A dataset for accelerated MRI reconstruction with dense image labels for quantitative clinical evaluation,” in *Thirty-fifth Conference on Neural Information Processing Systems Datasets and Benchmarks Track (Round 2)*, 2021. [Online]. Available: [https://openreview.net/forum?id=YDMFgD\\_qJuA](https://openreview.net/forum?id=YDMFgD_qJuA)
- [77] L. Pineda, S. Basu, A. Romero, R. Calandra, and M. Drozdal, “Active MR k-space sampling with reinforcement learning,” *arXiv preprint arXiv:2007.10469*, 2020.
- [78] R. Kates, D. Atkinson, and M. N. Brant-Zawadzki, “Fluid-attenuated inversion recovery (flair): clinical prospectus of current and future applications.” *Topics in magnetic resonance imaging: TMRI*, vol. 86, pp. 389–396, 1996.
- [79] D. P. Kingma and J. Ba, “Adam: A method for stochastic optimization,” *arXiv preprint arXiv:1412.6980*, 2014.
- [80] D. Ulyanov, A. Vedaldi, and V. Lempitsky, “Instance normalization: The missing ingredient for fast stylization,” *arXiv preprint arXiv:1607.08022*, 2016.
- [81] M. J. Cardoso, W. Li, R. Brown, N. Ma, E. Kerfoot, Y. Wang, B. Murrey, A. Myronenko, C. Zhao, D. Yang, V. Nath, Y. He, Z. Xu, A. Hatamizadeh, W. Zhu, Y. Liu, M. Zheng, Y. Tang, I. Yang, and A. Feng, “Monai: An open-source framework for deep learning in healthcare,” 11 2022.
- [82] S. Marcel and Y. Rodriguez, “Torchvision the machine-vision package of torch,” in *Proceedings of the 18th ACM International Conference on Multimedia*, ser. MM ’10. New York, NY, USA: Association for Computing Machinery, 2010, p. 1485–1488. [Online]. Available: <https://doi.org/10.1145/1873951.1874254>
- [83] M. Uecker, P. Lai, M. J. Murphy, P. Virtue, M. Elad, J. M. Pauly, S. S. Vasanawala, and M. Lustig, “ESpirit—an eigenvalue approach to autocalibrating parallel MRI: Where sense meets grappa,” *Magnetic Resonance in Medicine*, vol. 71, 2014.

## SUPPLEMENT A

### KNEE TISSUE SEGMENTATION EXPERIMENTS

In this section, we provide additional experimental results on a knee tissue segmentation problem in complement with the brain segmentation in Section IV-B.

**Dataset and setup** We consider segmenting four types of knee tissues: the patellar cartilage, the femoral cartilage, the tibial cartilage, and the meniscus. We use the *Stanford Knee MRI with Multi-Task Evaluation (SKM-TEA)* dataset [76], which contains pixel-level segmentation maps of the four tissues. Specifically, we use the raw 3D multi-coil  $k$ -space measurements of knee images and take 1D inverse Fourier transform along the left-to-right direction to obtain 2D  $k$ -space of sagittal slices.

**Baselines** We compare TACKLE<sub>seg.</sub> with the same baselines as the ones in the brain tissue segmentation experiments: LOUPE<sub>recon.</sub>, PD+UN<sub>recon.</sub>, TACKLE<sub>recon.</sub>, SemuNet.

**Results** We provide a quantitative comparison in Table VII and a boxplot comparison in Figure 11. Within the rectangle between each pair of methods in Figure 11, the top number is the percentage of samples that get improved and the bottom number is the  $p$ -value given by the paired samples t-test. With an improved architecture, TACKLE<sub>recon.</sub> already outperforms the other baselines. Nevertheless, the segmentation-oriented method TACKLE<sub>seg.</sub> achieves even better performance on both  $16\times$  and  $64\times$  accelerations. TACKLE<sub>seg.</sub> also significantly outperforms SemuNet on both acceleration ratios and has a much smaller

performance drop from  $16\times$  to  $64\times$  than SemuNet, indicating that the proposed approach is more robust to high acceleration ratios. We further provide some visual examples in Figure 12. The first row visualizes the input of the predictor by different methods, where each image is labelled by its PSNR value on the top right corner. The last row shows the predicted segmentation maps by different methods, where each prediction is labelled by its Dice score on the top right corner. The blue arrows point out the locations where TACKLE<sub>seg.</sub> provides more accurate reconstructions than other reconstruction-oriented baselines. We also provide a zoom-in on the region that contains the segmented tissues in the second row.

## SUPPLEMENT B

### IMPLEMENTATION DETAILS

In this section, we describe the implementation details of TACKLE and the baseline methods.

#### A. Further information on datasets and their preparation

For each dataset in Section IV, we randomly split the data into training, validation, and test sets *on the patient level*, which means that each validation or test slice comes from a patient whose images are not used for training.

1) *ROI-oriented reconstruction*: For this task, we use all images with Meniscus Tear (MT) annotations in the fastMRI(+) dataset [49], [70]. We follow the specific data splitting in [77], which results in 4,158 slices for training, 210 slices for validation, and 201 slices for testing. We crop the center of the  $k$ -space of each image and adjust the size and position of each bounding box accordingly.

2) *Brain tissue segmentation*: For this task, we use the 109-th coronal slice of each volume in the OASIS dataset [73]. The access to the dataset can be found here <sup>6</sup>. Specifically, we use the 4-label tissue-type segmentation maps, which include segments of cortex, white matter, subcortical gray matter, and cerebrospinal fluid (CSF). We split the data into 248 slices for training ( $\approx 60\%$ ), 82 slices for validation ( $\approx 20\%$ ), and 84 slices for testing ( $\approx 20\%$ ).

3) *Knee tissue segmentation*: For this task, we use all the sagittal slices in the SKM-TEA dataset [76] that contains all four segmentation labels (Patellar Cartilage, Femoral Cartilage, Tibial Cartilage, and Meniscus). We split the data into 2,935 slices for training ( $\approx 60\%$ ), 1,040 slices for validation ( $\approx 20\%$ ), and 987 slices for testing ( $\approx 20\%$ ).

4) *Pathology classification*: For this task, we use all the images acquired by the FLAIR sequence in the BRATS dataset [24] to detect the existence of the Glioma tumor. FLAIR stands for *fluid attenuated inversion recovery*, a kind of inversion recovery sequence that is commonly used for detecting various brain lesions due to its ability of suppressing the CSF signal and enhancing lesion-to-background contrast [78]. Empirically, we find that it is more accurate to detect the existence of the Glioma on FLAIR images than on images with the other contrasts in the BRATS dataset. We split the data into 30,495 slices for training ( $\approx 60\%$ ), 9,996 slices for validation ( $\approx 20\%$ ), and 10,353 slices for testing ( $\approx 20\%$ ).

<sup>6</sup><https://github.com/adalca/medical-datasets/blob/master/neurite-oasis.md>

TABLE VII  
COMPARISON OF AVERAGE TEST DICE SCORE ON THE SKM-TEA DATASET [76] FOR SEGMENTING FOUR KNEE TISSUES UNDER DIFFERENT ACCELERATION RATIOS ( $R$ )

$R$	PD+UN <sub>recon.</sub>	LOUPE <sub>recon.</sub>	SemuNet	TACKLE <sub>recon.</sub>	TACKLE <sub>seg.</sub>
16	0.7843	0.7888	0.8108	0.8232	<b>0.8532</b>
64	0.7486	0.6715	0.7741	0.8145	<b>0.8357</b>

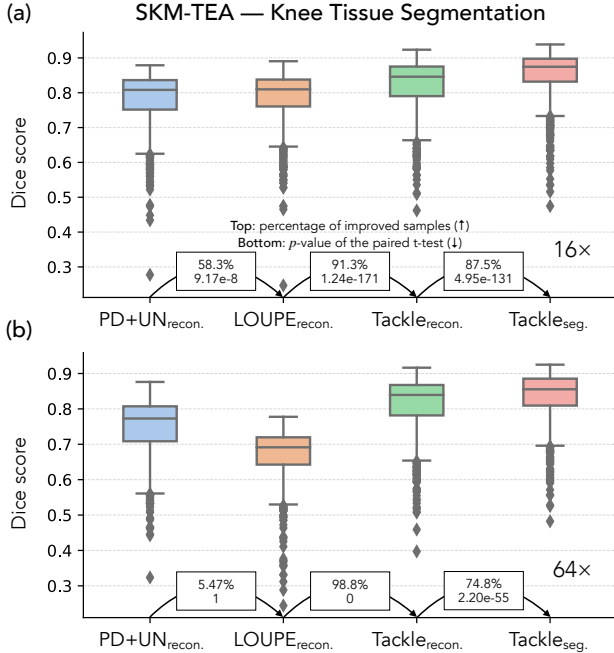


Fig. 11. Box plots of the knee tissue segmentation results under 16 $\times$  (a) and 64 $\times$  (b). Similar to the brain segmentation results, the proposed method TACKLE generally outperforms other baselines for both acceleration ratios. Within the rectangle between each pair of methods, the top number is the percentage of samples that get improved and the bottom number is the  $p$ -value given by the paired samples t-test. A higher percentage and lower  $p$ -value indicate a more significant improvement.

### B. Training and implementation details of TACKLE

1) *Training details*: For all experiments, we train the model using the Adam [79] optimizer with  $\beta_1 = 0.9$ ,  $\beta_2 = 0.999$  on a single NVIDIA A6000 GPU. We choose the best learning rate among  $\{1e-2, 1e-3, 1e-4\}$ , and trained all models until convergence (i.e. no improvement for 10 epochs on the validation set according to the task-specific evaluation metric). For instance, if a TACKLE<sub>seg.</sub> model achieves a higher Dice score on the validation set than all previous epochs on epoch 42, the model will be saved as a checkpoint. If it has no further improvement until epoch 52, then the training will be terminated and the saved checkpoint on epoch 42 will be used for reporting the final results.

The training of our proposed framework is conducted by retrospective subsampling on fully sampled measurements. The first module is the sampler, which requires no input and directly learns a matrix that contains the probability of sampling each  $k$ -space frequency. The output of the sampler is the subsampling mask  $\mathbf{m}$ , in which 1 represents the measurements to be sampled and 0 represents those not to be sampled. Sampling amounts to taking the element-wise product between  $\mathbf{m}$  and the fully sampled measurements  $\mathbf{k}$ , which gives us the subsampled

measurements  $\mathbf{y} := \mathbf{m} \odot \mathbf{k}$ . The retriever will then take the two-channel complex measurements  $\mathbf{y}$  as the input and output a single-channel real image  $\hat{\mathbf{x}}$ . In the multi-coil case,  $\mathbf{y}$  contains signals from multiple coils with different sensitivity maps and  $\hat{\mathbf{x}}$  is reconstructed by taking the root sum of square across all coils. For reconstruction tasks (full-FOV reconstruction and ROI-oriented reconstruction),  $\hat{\mathbf{z}} = \hat{\mathbf{x}}$  will be the final output for loss calculation and back-propagation. For downstream tasks beyond reconstruction, we feed  $\hat{\mathbf{x}}$  into an additional predictor which gives on a prediction  $\hat{\mathbf{z}}$ . In this case,  $\hat{\mathbf{z}}$  will be the final output for loss calculation and back-propagation.

2) *Retriever architecture*: Following the E2E-VarNet architecture [43], our retriever operates in  $k$ -space and contains 12 refinement steps, each of which includes a U-Net [59] with independent weights from each other. The update rule of the  $t$ -th refinement step is

$$\mathbf{k}^{t+1} = \mathbf{k}^t - \eta^t \text{diag}(\mathbf{m}) (\mathbf{k}^t - \mathbf{y}) + G^t(\mathbf{k}^t)$$

where  $\mathbf{m}$  is the subsampling mask,  $\mathbf{y}$  is the measurement,  $\mathbf{k}^t$  is the reconstructed  $k$ -space,  $\eta^t$  is a data consistency parameter, and  $G^t$  is the refinement module defined as

$$G^t(\mathbf{k}^t) := FE(\text{UN}^t(RF^{-1}\mathbf{k}^t)).$$

Here,  $E$  and  $R$  are the expand and reduce operations across all coils (see [43] for more details), and  $\text{UN}^t$  is the U-Net model at  $t$ -th step. Specifically, we use the standard U-Net [59] architecture with 2 input and output channels, 4 average down-pooling layers, and 4 up-pooling layers. The model starts with a 18-channel output for the input layer and doubles the number of channels with each downsampling layer. Between every two pooling layers are two convolution modules, each of which consists of a  $3 \times 3$  convolution, an instance normalization [80], and a LeakyReLU activation with negative slope of 0.2. The input to each U-Net is first normalized to zero mean and standard deviation of 1 before being fed into the network, and will be normalized back to the original mean and standard deviation after passing through the network. After 12 refinement steps, the final output layer of the retriever is an inverse Fourier transform followed by a root-sum-squares reduction for each pixel over all coils. The output of the retriever is a batch of single-channel images. For reconstruction tasks, a loss function will be directly applied to the output. For non-reconstruction tasks, there is an additional predictor module.

3) *Predictor architecture*: For tissue segmentation tasks, the predictor is a U-Net model that has the same architecture as the refinement network described above except for the following differences: There are 1 input channel and  $c$  output channels (where  $c$  is the number of segmentation classes). The model starts with a 64-channel output for the input layer. The convolution modules use Parametric ReLU activation. There is no normalization after the output. We used the U-Net implementation in the MONAI package [81]. For the pathology classification task, the predictor is a standard ResNet18 model except for using 1 input channel and 2 output dimensions. We normalize the input to zero mean and standard deviation of 1 before feeding it into the network. We used the ResNet implementation in the torchvision package [82].

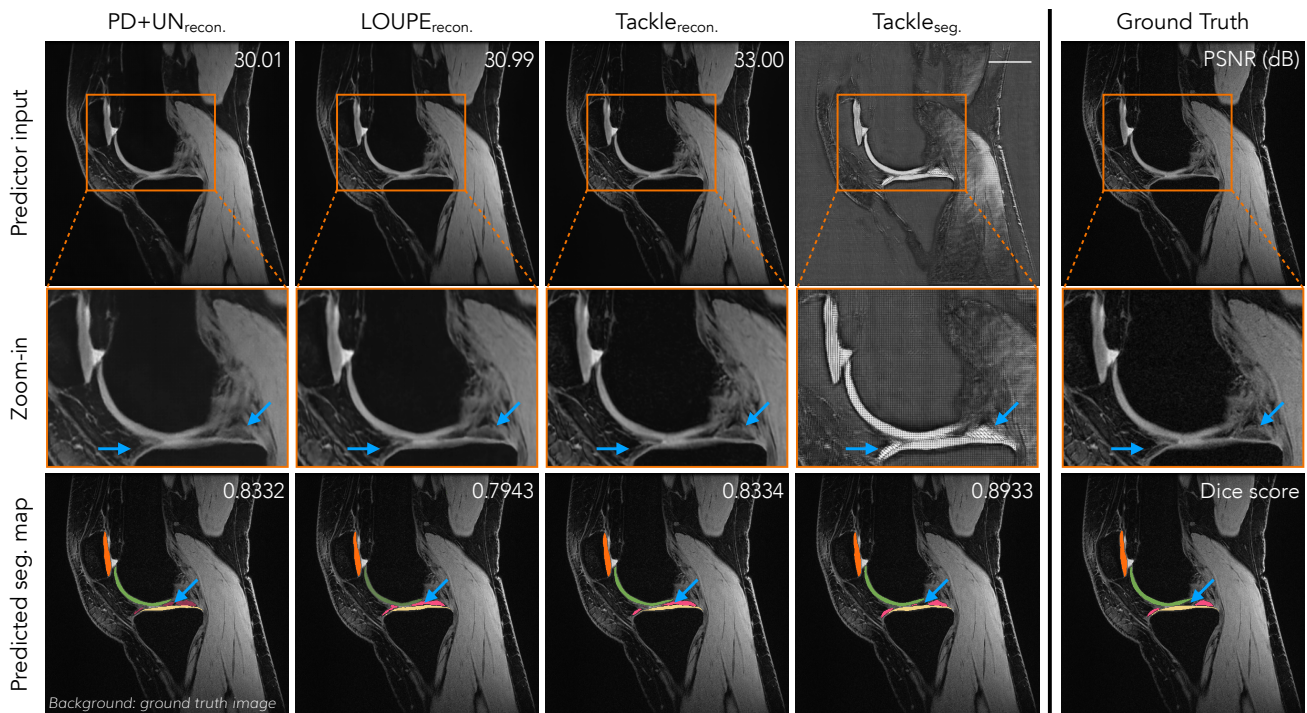


Fig. 12. Comparison of segmentation results under  $16\times$  acceleration on one sample of the SKM-TEA dataset. We show the input of the predictor in the first row, a zoom-in on the region that contains the tissues to be segmented in the second row, and the output of the predictor in the third row. Similar to the brain segmentation results, TACKLE (co-design) method circumvents the typical “reconstruction” in terms of point-wise similarity with the ground truth image. Instead, it learns an anatomically accurate feature map, which enables better segmentation prediction than other baselines both for this sample and on average over the test set (Table VII). This is similar to the brain segmentation results in Section IV-B and highlights the need for learning task-specific strategies.

### C. Pre-select region and sensitivity map estimation

Among all the datasets considered in this manuscript, fastMRI(+) [49], [70] and SKM-TEA [76] contain multi-coil  $k$ -space measurements. Reconstruction from multi-coil  $k$ -space data requires estimation of the coil sensitivity maps, i.e.  $S_i$  in (2), using the central low-frequency region of the  $k$ -space, called the Auto-Calibration Signal (ACS). We set the ACS region as a square around the DC component that contains  $1/8$  of the subsampling budget. For example, if a dataset contains  $k$ -space measurements of size  $256 \times 256$ , for  $8\times$  acceleration, we will select the center  $32 \times 32$  low frequencies as the ACS. We also include the pre-determined ACS region for single-coil  $k$ -space experiments because we find that it stabilizes the training of some baselines.

Given the ACS, we estimate coil sensitivity maps using the Sensitivity Map Estimation (SME) module introduced in [43]. In contrast to the ESPIRiT algorithm [83], SME estimates the sensitivity maps with a CNN applied to each coil image independently. The architecture of the CNN in SME is the same as the U-Net in each E2E-VarNet cascade, except with an 8-channel output instead of an 18-channel output for the input layer.

### D. Further details on the implementation of SemuNet [56]

For the brain and knee segmentation tasks, we compare the proposed method with SemuNet [56]. Originally demonstrated for a brain segmentation task, it also aims to jointly optimize a subsampling mask, a reconstructor, and a task predictor for the downstream accuracy. SemuNet uses a hybrid of  $\ell_1$  loss for

reconstruction and cross-entropy loss for segmentation. Since the code of SemuNet is not released, we have tried to reproduce the results in the original paper to our best efforts. Specifically, we follow their proposed loss function and architecture of the sampler, the residual U-Net reconstructor, and a U-Net predictor. We follow the original paper to use an Adam optimizer [79] and not pre-select low-frequency measurements. However, since our tasks and datasets are different from those in [56], we empirically find that the learning rate and the parameter  $\lambda$  that adjusts the trade off between the two losses are suboptimal for our settings. Therefore, we conduct a grid search on the learning rate in  $\{0.001, 0.005, 0.01, 0.05, 0.1, 0.5, 1, 5\}$  and  $\lambda \in \{0.0001, 0.001, 0.01\}$ . For both  $16\times$  and  $64\times$  accelerations, we choose the best combination of parameters based on the performance on the validation set, and report the Dice score on the test set.

## SUPPLEMENT C

### SUBSAMPLING SETUP AND IMPLEMENTATION

In this work, we optimize the subsampling mask  $m$  over all 2D subsampling patterns. We realize 2D subsampling patterns in practice by subsampling in the two phase encoding dimensions of a 3D Cartesian sequence based on the 2D pattern, as illustrated in Figure 13. We denote the number of trajectories along  $k_y$  and  $k_z$  (the two phase encoding directions) as  $n_{k_y}$  and  $n_{k_z}$ , respectively. For the fully sampling scenario, one needs to sequentially sample a total of  $n_{k_y} n_{k_z}$  trajectories, which could take a long time to acquire in practice. Given a 2D subsampling mask  $m$ , we subsample in the  $k_y$ - $k_z$  plane according to  $m$ . If  $m$  has an acceleration ratio of  $R$ , the



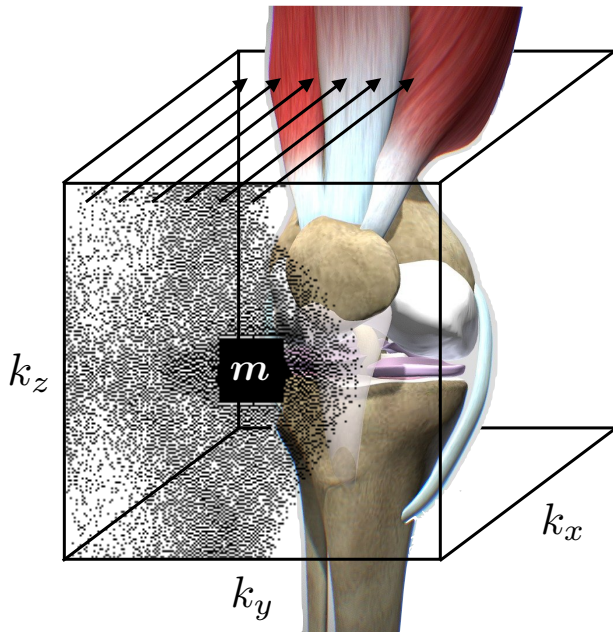


Fig. 13. Conceptual illustration of the subsampling setup with a knee example. The back dots on the  $k_y$ - $k_z$  plane represents  $k$ -space trajectories along  $k_x$ , which are illustrated by the black arrows. We consider subsampling in the two phase-encoding dimensions ( $k_y$  and  $k_z$ ) of a 3D Cartesian sequence, where the subsampling pattern  $m$  is learned from data for some specific downstream task.

subsampling sequence only takes  $n_{k_y} n_{k_z} / R$  trajectories and the acquisition time will be reduced by a factor  $R$  in practice. One can obtain the slice-wise 2D  $k$ -space measurements  $\mathbf{y}$  by taking the 1D inverse Fourier Transform of the raw 3D  $k$ -space data along  $k_x$ . We have implemented a  $4\times$ -accelerated version of the sequence we used in Section V on the Siemens IDEA sequence programming platform, using the subsampling scheme we described above. Figure 10 demonstrates that the prospective subsampling version of our learned sequence achieves the same level of visual quality as the fully sampling version but only takes a quarter of the scan time. This result highlights the real-world practicality of our approach.

#### SUPPLEMENT D

##### ADDITIONAL VALIDATION ON OUT-OF-DISTRIBUTION DATA

In Section IV-A, we showed that  $\text{TACKLE}_{\text{ROI}}$  improves the reconstruction of ROIs that contain the meniscus tear (MT). In practice, it is likely that a healthy subject or someone with a different pathology lesion from the meniscus tear will get scanned. So it is important that the learned sequence should also generalize to out-of-distribution subjects. Here we take our trained  $\text{TACKLE}_{\text{ROI}}$  models with  $4\times$ ,  $8\times$ , and  $16\times$  accelerations from our ROI reconstruction experiments, and directly test them on images that do not contain the meniscus tear, without additional fine-tuning. The results are summarized in Table VIII.

Although it is not surprising that  $\text{TACKLE}_{\text{ROI}}$  performs better on the in-distribution data (samples w/ MT), we want to point out that the two numbers above correspond to two different test sets and are thus not directly comparable. The main takeaway is that  $\text{TACKLE}_{\text{ROI}}$  can robustly recover samples without MT,

TABLE VIII  
COMPARISON OF  $\text{TACKLE}_{\text{ROI}}$  ON IN- AND OUT-OF-DISTRIBUTION SAMPLES UNDER VARIOUS ACCELERATION RATIOS ( $R$ )

Metric	$R$	Samples w/ MT (in-distribution)	Samples w/o MT (out-of-distribution)
PSNR (dB)	4	37.65	36.92
	8	33.28	32.88
	16	32.06	31.74

even if it is trained on samples with MT. As discussed in Section IV-A,  $\text{TACKLE}_{\text{ROI}}$  improves the ROI reconstruction by trading off  $k$ -space frequencies for the local anatomy to attain improved resolution. We find that such a strategy can lead to satisfactory recovery quality even when the underlying subject does not contain the target pathology.